J. Fluid Mech. (2024), *vol*. 990, A6, doi:10.1017/jfm.2024.351

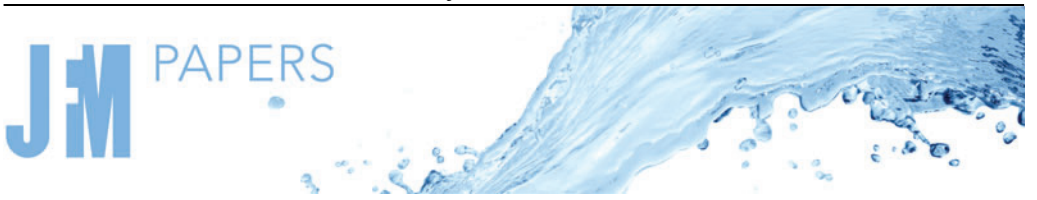

Pore-scale study of CO_2 desublimation and sublimation in a packed bed during cryogenic carbon capture

Timan Lei[1], Kai H. Luo[1,†], Francisco E. Hernández Pérez[2], Geng Wang[1], Junyu Yang[1], Juan Restrepo Cano[2] and Hong G. Im[2]

[1]Department of Mechanical Engineering, University College London, Torrington Place, London WC1E 7JE UK

[2]CCRC, Physical Science and Engineering, King Abdullah University of Science and Technology, Thuwal 23955-6900 Saudi Arabia

(Received 7 August 2023; revised 28 March 2024; accepted 1 April 2024)

Cryogenic carbon capture (CCC) is an innovative technology to desublimate CO_2 out of industrial flue gases. A comprehensive understanding of CO_2 desublimation and sublimation is essential for widespread application of CCC, which is highly challenging due to the complex physics behind. In this work, a lattice Boltzmann (LB) model is proposed to study CO_2 desublimation and sublimation for different operating conditions, including the bed temperature (subcooling degree ΔT_s), gas feed rate (Péclet number Pe) and bed porosity (ψ). The CO_2 desublimation and sublimation properties are reproduced. Interactions between convective CO_2 supply and desublimation/sublimation intensity are analysed. In the single-grain case, Pe is suggested to exceed a critical value Pe_c at each ΔT_s to avoid the convection-limited regime. Beyond Pe_c, the CO_2 capture rate (v_c) grows monotonically with ΔT_s, indicating a desublimation-limited regime. In the packed bed case, multiple grains render the convective CO_2 supply insufficient and make CCC operate under the convection-limited mechanism. Besides, in small-ΔT_s and high-Pe tests, CO_2 desublimation becomes insufficient compared with convective CO_2 supply, thus introducing the desublimation-limited regime with severe CO_2 capture capacity loss (η_d). Moreover, large ψ enhances gas mobility while decreasing cold grain volume. A moderate porosity ψ_c is recommended for improving the CO_2 capture performance. By analysing v_c and η_d, regime diagrams are proposed in ΔT_s–Pe space to show distributions of convection-limited and desublimation-limited regimes, thus suggesting optimal conditions for efficient CO_2 capture. This work develops a viable LB model to examine CCC under extensive operating conditions, contributing to facilitating its application.

† Email address for correspondence: k.luo@ucl.ac.uk

Key words: convection in porous media, solidification/melting, coupled diffusion and flow

1. Introduction

Climate change is taking place at an unprecedented pace and its impact is being felt across the world with rising sea levels, severe heat waves and more frequent and intense natural disasters (Letelier *et al.* 2023; Liu *et al.* 2023). As one of the most pressing environmental issues, climate change is broadly reported to be caused by human activities such as the burning of fossil fuels and deforestation, which lead to critical emissions and buildup of CO_2 in the atmosphere (Mac Dowell *et al.* 2017; Zhou, Jin & Luo 2020; Ren & Kloker 2022; Hu, Xu & Yang 2023). Numerous studies have emphasized the necessity of taking immediate actions to reduce global greenhouse gas emissions (primarily CO_2) to meet the 1.5 °C target of the Paris Agreement (Susskind *et al.* 2020; Solomon 2023). Therefore, various carbon capture technologies have been developed to separate CO_2 from anthropogenic emissions, including chemical absorption, physical adsorption, membrane separation and cryogenic capture (Song *et al.* 2019; Nocito & Dibenedetto 2020; Naquash *et al.* 2022; Lei *et al.* 2023).

Cryogenic carbon capture (CCC), as an innovative technology, cools the industrial flue gas to cryogenic temperatures (usually below −100 °C) and, thus, desublimates the CO_2 component. Consequently, the desublimated CO_2 is separated in pure from other gas components, based on the difference in their freezing points (bin Ab Halim 2013; Maqsood *et al.* 2014). This desublimation-based CCC offers several benefits, including high capture efficiency, low chemical usage and flexible application, which make it hold significant application perspectives and research interests (Babar *et al.* 2018, 2021; Font-Palma, Cann & Udemu 2021). Although CCC has been successfully tested in several pilot projects, it is still in the nascent stage of commercial applications due to some operational challenges (Pan, Clodic & Toubassy 2013; Gallucci & van Sint Annaland 2015). For example, cooling flue gas to extremely low temperatures requires a significant amount of energy, which may make CCC less cost effective than other mature technologies (i.e. chemical absorption and physical adsorption). Low temperatures also have the tendency to cause equipment corrosion. Additionally, inappropriate gas feed rates and heat exchanger units pose risks, such as gas breakthrough, flow channel plug and even premature termination of CCC. Therefore, to address these operational concerns and improve the commercial feasibility of CCC, it is essential to conduct an in-depth investigation of the multiphysics and desublimation kinetics behind CCC.

During the operation of the desublimation-based CCC, the flue gas, containing multiple components, flows unsteadily through the void channels among heat exchangers. As the flue gas is cooled and the heat exchanger is heated, CO_2 is first desublimated and then partially sublimated (Debnath *et al.* 2019). The intensity of CO_2 desublimation and sublimation determines the CO_2 capture capacity and efficiency of CCC. Therefore, the control of these two aspects (i.e. CO_2 desublimation and sublimation) is vital in the development of an effective CCC. However, the problem of CO_2 desublimation and sublimation during CCC incorporates multiple and fully coupled physics, i.e. fluid dynamics, mass transfer mechanisms, conjugate heat transfer between the gas and solid phases, desublimation and sublimation kinetics and solid phase evolutions (Lei *et al.* 2023).

To understand such a complex problem, experiments have been designed and conducted. Tuinier *et al.* (2010) proposed a novel CCC system using a dynamically operated packed

bed. The carbon capture capacity of the system was experimentally investigated for N_2/CO_2 mixtures at atmospheric pressure. However, this system applied a single bed and worked in a discontinuous cycle of three steps: cooling, capture and recovery. To achieve the continuous capture of CO_2, they further created a CCC system comprising three beds to operate the three steps in parallel (Tuinier, Hamers & van Sint Annaland 2011*a*; Tuinier, van Sint Annaland & Kuipers 2011*b*; Tuinier & van Sint Annaland 2012). Their experiments showed that a lower initial bed temperature and a higher CO_2 concentration could reduce the operating cost. For example, the 5 % CO_2 case yielded a cost of \$95.7/ton_{CO_2}, which decreased notably to \$59.8/ton_{CO_2} for the 10 % CO_2 case. In addition, compared with two competing technologies (i.e. amine absorption and membrane separation), the improved CCC was shown to be the preferred option if a cold source was available at low costs. Nevertheless, these CCC systems were designed to purify flue gases with relatively low CO_2 contents (i.e. up to 30 % CO_2), and their operations were constrained to the atmospheric pressure. Taking this into account, Ali *et al.* (2014, 2016) used the multiple cryogenic desublimation based pipeline network to achieve the removal of H_2O and CO_2 from the natural gas under high CO_2 concentrations and high pressures (i.e. up to 100 % CO_2 and 20 bar).

Another CCC system based on commercial Stirling coolers (SCs) was developed for gas cooling, CO_2 desublimation and CO_2 capture, in which multiple SCs were applied to serve as heat exchangers (Song *et al.* 2012*b*; Song, Kitamura & Li 2012*a*; Song *et al.* 2013; Song, Kitamura & Li 2014). After extensive experiments on cooling fins of 15 mm length, they suggested the gas feed rate of 2 L min^{-1} and the SC temperature of $-20\,^{\circ}C$ for the gas cooling stage to obtain the optimal performance (i.e. 85 % CO_2 recovery at 3.4 MJ $kg^{-1}_{CO_2}$). Due to the cost and difficulty in achieving extremely low temperatures (i.e. below $-100\,^{\circ}C$), however, optimal operating conditions for the CO_2 desublimation stage were not determined. In addition to these fixed-bed or fixed-SC CCC systems, the moving-bed CCC system was recently proposed (Willson *et al.* 2019; Cann, Font-Palma & Willson 2021*a*,*b*; Font-Palma 2021). The packed bed applied moving packing materials to continuously remove materials covered by desublimated CO_2, thus realizing the continuous capture of CO_2 without introducing multiple packed beds. Experiments were carried out to determine an adequate bed velocity and optimize the carbon capture behaviours.

In these existing experiments, the feasibility of various CCC concepts has been validated and the CO_2 capture performance has been assessed for different operating conditions. Nevertheless, due to the significant operational expenses, only a narrow range of operating parameters were examined in experiments. In light of this limitation, numerical simulations were performed at the same time to investigate the performance of CCC for extensive operating conditions. Tuinier *et al.* (2010, 2011*a*) proposed a one-dimensional (1-D) pseudo-homogeneous model to simulate the desublimation and sublimation of CO_2. By comparing with experiments, they determined the mass transfer rate constant for CO_2 desublimation and sublimation. Their numerical results confirmed the experimental observation that the desublimation of CO_2 raised the bed temperature to an equilibrium level of $-(93\text{–}98)\,^{\circ}C$. They also demonstrated that an initial bed temperature above the threshold of $-120\,^{\circ}C$ could exponentially reduce the amount of CO_2 captured (Tuinier *et al.* 2011*b*). For instance, for a fed mixture with 10 % CO_2, the increased bed temperature from $-120\,^{\circ}C$ to $-110\,^{\circ}C$ could diminish the recovered CO_2 from 90 % to 12 %. By introducing a new mass transfer scheme, this 1-D model was improved to consider both the CO_2 desublimation on the gas–solid interface and the CO_2 nucleation inside the gas phase (Debnath *et al.* 2019). This improved model was able to evaluate the CO_2 capture capacity, predict operating risks (e.g. chocking), and identify

the saturation point between capture and recovery steps. This 1-D model was recently extended to consider the energy balance for moving heat exchangers (Cann & Font-Palma 2023).

On the other hand, a two-dimensional (2-D) quasi-steady model was developed to solve the heat and mass transfer during the desublimation and sublimation of CO_2 (Song *et al.* 2012*b*,*a*). The frosted CO_2 layer was found to enhance the heat resistance and increase the frost surface temperature. For instance, as the frost thickness increased from 0 mm to 3 mm, the thermal conductivity of frost escalated from 0 to 0.4 $W\,mK^{-1}$ and the temperature rose from $-106.3\,^{\circ}C$ to $-98\,^{\circ}C$ (Song *et al.* 2013). This 2-D model was then advanced to consider heat integration, membrane capture, pressure recovery and cold thermal energy utilization units, showing the decreased energy consumption of these improved CCC systems (Song *et al.* 2017*a*,*b*; Sun *et al.* 2021). It is emphasized that the above 1-D and 2-D models were based on a unified velocity profile and ignored impacts of the unsteady gas flow. Consequently, a 1-D transient model was proposed to reveal the detailed CO_2 desublimation characteristics, with the unsteady gas flow, mass transfer and energy conservation being included (Wang *et al.* 2018*a*). The model was validated by experimental data and exhibited improved accuracy when incorporating the desublimated solid CO_2 layer (SCL) in an annular tube. In addition, the lower gas feed rate and the higher CO_2 concentration were found to yield the higher carbon capture rate (e.g. the CO_2 capture rate was upgraded from 40 % for 1800 $ml\,s^{-1}$ to 100 % for 300 $ml\,s^{-1}$).

These existing models have simulated the desublimation and sublimation properties of CO_2, and evaluated the carbon capture performance of CCC for a certain range of operating conditions. Despite these achievements, the limitations of either 1-D or quasi-steady assumptions make existing models inadequate in capturing the multiple physics and complex interactions behind CCC. In addition, these existing models were constructed on volume-averaged scales. As a result, intricate structures of the desublimated CO_2 at the pore scale were ignored, conjugate heat transfer between the gas and solid phases was simplified, the random growth and consumption of desublimated CO_2 were neglected, and the porous structure of the packed bed was disregarded. Furthermore, in previous numerical studies, heat and mass transfer coefficients were estimated by empirical correlations, the accuracy of which depends on a prior pore-scale knowledge base (Xu *et al.* 2018*a*,*b*, 2022). Therefore, a pore-scale model is crucial for a comprehensive study of CO_2 desublimation and sublimation during CCC, which is currently missing.

Over the past three decades, the lattice Boltzmann (LB) method has been extensively developed for simulating complex fluid flows with phase change and chemical reactions at the pore scale (Li *et al.* 2016; Lei, Luo & Wu 2019; Chen *et al.* 2022; Sawant, Dorschner & Karlin 2022). Accordingly, there exist plentiful LB models for separately investigating the multiple physics behind CO_2 desublimation and sublimation at the pore scale, including the unsteady fluid flow (Wang *et al.* 2018*b*; Shi, Wu & Shan 2021; Li & Shan 2023), species transport (Sawant, Dorschner & Karlin 2021), conjugate heat transfer (Karani & Huber 2015; He *et al.* 2019), reactive fluid–solid interface (Zhang *et al.* 2012, 2019) and solid structure evolution (Chen *et al.* 2014, 2020). However, the combination and interactions of these complex physics have not been achieved by a single LB model, which is indeed challenging.

To fill this gap, we recently formulated a pore-scale CCC modelling framework based on the LB method, incorporating the unsteady gas flow, conjugate heat transfer, desublimation kinetics and solid CO_2 generation (Lei *et al.* 2023). The model was successfully applied to identify different CO_2 desublimation regimes, albeit constrained to a single packing material and fixed packing temperatures. In this work, the LB model is extended to

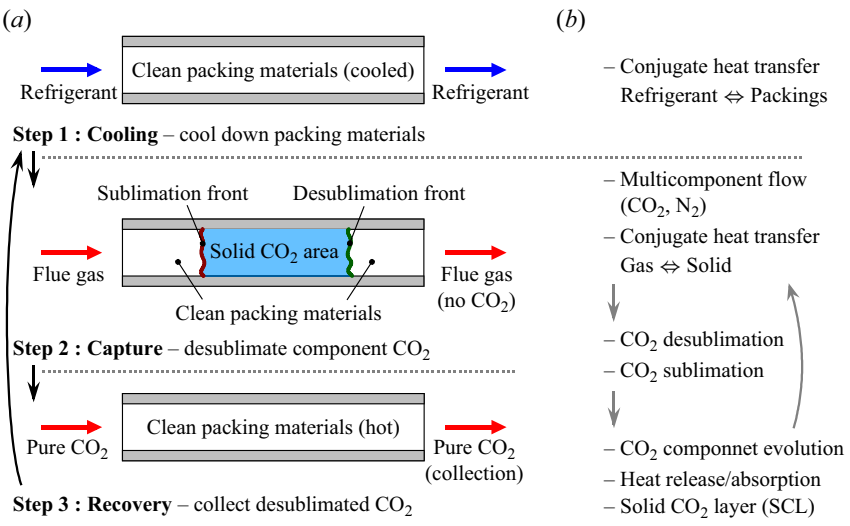

Figure 1. The schematic descriptions of (*a*) the operation of CCC in a packed bed and (*b*) the underlying multiple physics.

incorporate both CO_2 desublimation and sublimation in a packed bed, considering the consumption of solid CO_2 as the packed bed is heated. By evaluating the carbon capture performance for different operating conditions, this study aims to improve the understanding of CCC and shed light on the optimal operating conditions.

2. Physical and mathematical models

The operation of CCC in a packed bed is schematically depicted in figure 1(*a*), which follows a circle of three steps: cooling, capture and recovery (Tuinier *et al.* 2011*b*; Ali *et al.* 2014; Babar *et al.* 2021). During the cooling step, a refrigerant (e.g. refrigerated N_2, cleaned flue gas, evaporated liquified natural gas) feeds into the packed bed and cools packing materials below the freezing point of CO_2. The refrigerant exits the bed after the cooling process, and it can either be released into the atmosphere or recycled to the bed inlet via a cooler. Then, the CCC system enters the capture step and the feed is switched to the warm flue gas. In the cooled packed bed the component CO_2 is desublimated and a front of the desublimated CO_2 (or desublimation front, l_d) is formed. Meanwhile, as the packing grains are heated by the warm flue gas, previously desublimated CO_2 is sublimated to form a sublimation front (l_s) behind l_d. Once the fed CO_2 starts to leave the bed outlet, the packed bed becomes saturated and the recovery step begins. The feed is changed to the warm CO_2 gas, which promotes the continuous sublimation of solid CO_2. The sublimated CO_2 exits the bed and is collected for cycling or subsequent applications. Once all the solid CO_2 is recovered, the CCC system returns to the cooling step. The CO_2 capture and recovery steps usually have a longer duration compared with the cooling period.

In the cooling step, CCC is dominated by the heat transfer between the refrigerant and the packing materials, with no separation of CO_2 being introduced. During the following capture and recovery of CO_2, the more complex and fully coupled multiphysics takes part and must be considered. On the one hand, the multicomponent gas flow in channels and conjugate heat transfer between the gas and solid phases (i.e. solid packing materials and solid CO_2) are introduced. On the other hand, the desublimation and

sublimation of CO_2 take place and modify the solid structure, multicomponent gas flow and gas compositions. Meanwhile, CO_2 desublimation and sublimation are exothermic and endothermic, respectively, thus affecting the heat transfer. Such changes in the local CO_2 composition and temperature, in turn, control the desublimation and sublimation rates. Therefore, the multicomponent gas flow, conjugate heat transfer, solid structure evolution and desublimation and sublimation kinetics are fully coupled. The interactions of these multiple physics are sketched in figure 1(*b*). Considering that the CO_2 capture performance of CCC is mainly determined by the desublimation and sublimation of CO_2, this study focuses on the capture and recovery steps.

Before constructing governing equations for describing the desublimation and sublimation of CO_2 during CCC at the pore scale, some simplifications and assumptions are made as follows: (1) this work investigates the capture and recovery of CO_2 without detailing the cooling of packing materials; (2) the flue gas, treated as a mixture of CO_2 and N_2, obeys the ideal gas law and is incompressible and neutrally buoyant; (3) Fick's law is applied to describe the species mass diffusion; (4) the mass transfer rate of CO_2 desublimation and sublimation is proportional to the local deviation from the gas–solid equilibrium; (5) physical properties of the gas and the solid phases are set as constants in relation to the initial condition; and (6) a cryogenic bed packed with multiple grains of a uniform diameter is considered, the movement of packing grains are neglected, and the bed porosity equals the experimental value (Ali *et al.* 2014).

Under these premises, a sample cryogenic packed bed with porosity ψ is depicted in figure 2(*a*). The computational domain is $0 \leq x \leq l_x$ and $0 \leq y \leq l_y$, wherein a staggered array of circular grains with a uniform diameter d is encompassed. From the bed inlet, the incompressible flue gas is injected at temperature T_0, pressure p_0 and velocity $\boldsymbol{u}_0$. Initially, the flue gas consists of CO_2 and N_2, having mass fractions Y_0 and $(1 - Y_0)$, respectively. The temperature of packing grains is set to T_w at first, which is above the freezing point of N_2 but below that of CO_2. Hence, after injection, N_2 flows through the domain without phase change, while CO_2 is partially desublimated to form an SCL on the surface of the packing grains. The CO_2 desublimation is exothermic and expressed as

$$CO_2\,(g) \rightarrow CO_2\,(s) + Q_d. \tag{2.1}$$

Here, Q_d is the heat released from CO_2 desublimation, and the gas and solid phases of CO_2 are denoted by g and s, respectively.

Due to the exothermic desublimation process and the heat transfer between the gas stream and solid packing grains, the temperature of the solid phases is locally raised to the freezing point of CO_2. Consequently, the captured SCL starts to sublimate as

$$CO_2\,(s) + Q_s \rightarrow CO_2\,(g)\,. \tag{2.2}$$

Both the CO_2 desublimation and the incoming warm flue gas contribute to the heat Q_s for sublimation.

For such desublimation and sublimation processes, the mass transfer rate between the gaseous CO_2 and the solid CO_2 is estimated as (Tuinier *et al.* 2010; Debnath *et al.* 2019)

$$m_r = \begin{cases} k_r\,(y_i p - p_e) & \text{if } (y_i p > p_e, y_i > 0)\,, \\ k_r\,(y_i p - p_e)\,A & \text{if } \left(y_i p < p_e, A = \dfrac{m_i}{m_i + 0.1} > 0\right), \\ 0 & \text{if } \{(y_i p > p_e,\ y_i = 0) \text{ or } (y_i p < p_e, A = 0)\}. \end{cases} \tag{2.3}$$

Depending on the sign of m_r, either CO_2 desublimation ($m_r > 0$) or CO_2 sublimation ($m_r < 0$) occurs. Here, k_r is the mass desublimation rate constant, m_i is the mass of

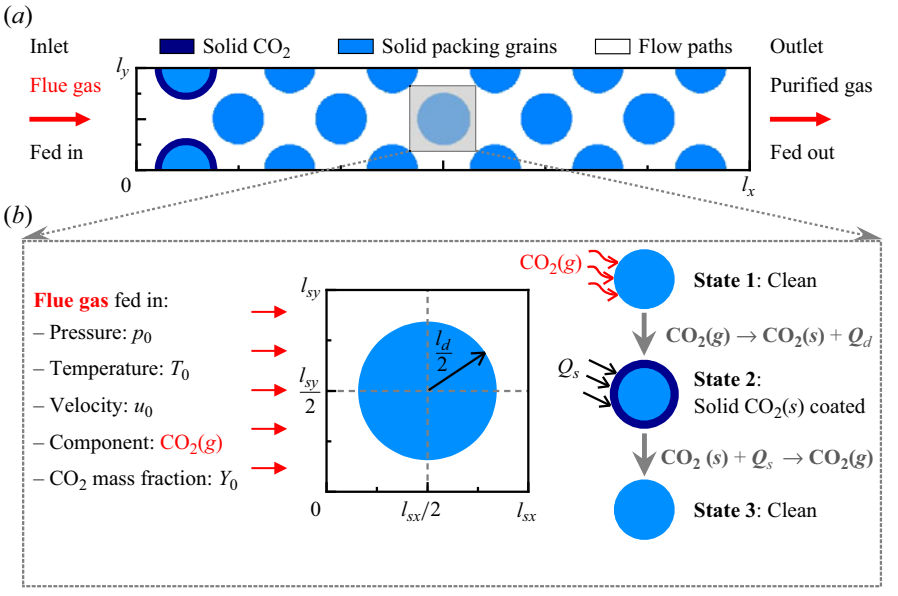

Figure 2. The schematic diagrams of (*a*) the cryogenic packed bed for simulation and (*b*) CO_2 desublimation and sublimation on a single packing grain at the pore scale.

desublimated CO_2 per unit volume and p is the flue gas pressure. The mole fraction of CO_2 is calculated as

$$y_i = \frac{M}{M_{CO_2}} Y, \quad \text{with } \frac{1}{M} = \frac{Y}{M_{CO_2}} + \frac{1-Y}{M_{N_2}}, \tag{2.4}$$

where Y is the mass fraction of CO_2 in the flue gas. Here M, M_{CO_2} and M_{N_2} are molecular weights of the flue gas, CO_2 and N_2, respectively. In (2.3), for the mass transfer rate m_r, the equilibrium pressure between the gas and the solid phases corresponding to the local temperature T is determined by an empirical correlation as (Tuinier *et al.* 2010)

$$p_e = \exp\left(10.257 - \frac{3082.7}{T} + 4.08 \ln T - 2.2658 \times 10^{-2} T\right). \tag{2.5}$$

The units of p_e and T are Pascal (Pa) and Kelvin (K), respectively.

From the desublimation and sublimation processes, the released heat Q_d and the absorbed heat Q_s are calculated as

$$Q_{d,s} = m_r a_r h_r, \tag{2.6}$$

with h_r being the enthalpy change of CO_2 desublimation and a_r being the specific surface area per unit volume. Details on the calculation of a_r and its sensitivity are provided in the supplementary material available at https://doi.org/10.1017/jfm.2024.351. By using (2.6), either Q_d for desublimation ($m_r > 0$) or Q_s for sublimation ($m_r < 0$) can be calculated. During CO_2 desublimation and sublimation, the pore structure of the solid phases changes with the generation and consumption of SCL on the surface of the packing grains. This structure evolution is tracked by the mass balance equation for the solid CO_2 as

(Kang *et al.* 2014)

$$\rho_s \partial_t V_s = m_r a_r V_r, \tag{2.7}$$

where V_s and ρ_s represent the volume and density of solid CO_2, respectively, and V_r is the active volume for desublimation.

From the mass transfer scheme in (2.3), the following three scenarios may occur at the interface between the gas and solid phases I.

(i) At the interface I_d, the partial pressure and mass fraction of the component CO_2 satisfy the criterion ($y_i p > p_e$, $y_i > 0$). So, m_r is positive (i.e. $m_r > 0$) and CO_2 desublimation takes place. During this process, gaseous CO_2 is consumed, heat Q_d is released and SCL is generated.

(ii) At the interface I_s satisfying the criterion ($y_i p < p_e, A > 0$), m_r becomes less than 0 (i.e. $m_r < 0$) and SCL is sublimated to produce gaseous CO_2. Such a process brings about the generation of gaseous CO_2, the absorption of heat Q_s and the consumption of the SCL.

(iii) At the interface I_n with ($y_i p > p_e$, $y_i = 0$) or ($y_i p < p_e, A = 0$), m_r equals 0. Thus, neither the desublimation nor sublimation of CO_2 happens.

Note that the calculation of m_r in (2.3) can be conveniently replaced by other expressions if necessary. In this study, $I_{d,s}$ (i.e. I_d and I_s) and I_n are referred to as active and inactive boundaries, respectively.

Based on the above assumptions and definitions, a set of governing equations is built up to model the desublimation and sublimation of CO_2 during CCC at the pore scale. That includes the continuity equation (2.8), the incompressible Navier–Stokes equation (2.9) and the component conservation equation (2.10) for the flue gas stream in flow paths, as well as the energy balance equation (2.11) for heat transfer in both flow paths (i.e. flue gas) and solid phases (i.e. solid packing materials and solid CO_2). These equations are expressed as follows:

$$\nabla \cdot \boldsymbol{u} = 0, \tag{2.8}$$

$$\rho_g \frac{\partial \boldsymbol{u}}{\partial t} + \rho_g \nabla \cdot (\boldsymbol{u}\boldsymbol{u}) = -\nabla p + \rho_g \nabla \cdot (\nu \nabla \boldsymbol{u}), \tag{2.9}$$

$$\frac{\partial Y}{\partial t} + \nabla \cdot (Y\boldsymbol{u}) = \nabla \cdot (D \nabla Y), \tag{2.10}$$

$$\frac{\partial}{\partial t}\left(\rho c_p T\right) + \nabla \cdot \left(\rho c_p T \boldsymbol{u}\right) = \nabla \cdot \left(\rho c_p \alpha \nabla T\right) + Q. \tag{2.11}$$

Here, $\boldsymbol{u} = (u, \ v)$, ρ_g and ν are the gas velocity, density and kinematic viscosity, respectively; t is the time and D is the diffusion coefficient of CO_2; ρ, c_p and α are the local density, specific heat capacity at constant pressure and thermal diffusivity, respectively. The heat Q can be either the released desublimation heat Q_d or the absorbed sublimation heat Q_s.

The desublimation and sublimation of CO_2 take place at the active gas–solid interface I_d and I_s, respectively. Such processes are described by boundary conditions as

$$\boldsymbol{u}^{I_{d,s}} = (0, 0)\,, \tag{2.12}$$

$$\boldsymbol{n} \cdot D\rho_g \nabla Y^{I_{d,s}} = m_r, \tag{2.13}$$

$$\left.\begin{aligned} T^{I_{d,s},+} &= T^{I_{d,s},-}, \\ \boldsymbol{n} \cdot \left(k\nabla T + \rho c_p \boldsymbol{u} T\right)^{I_{d,s},+} &= \boldsymbol{n} \cdot \left(k\nabla T + \rho c_p \boldsymbol{u} T\right)^{I_{d,s},-} + q. \end{aligned}\right\} \tag{2.14}$$

In the above equations, $\boldsymbol{n}$ is the interface normal pointing to the gas phase, $+$ and $-$ denote parameters on either side of $I_{d,s}$, $k = \alpha\rho c_p$ is the thermal conductivity and q is the heat flux caused by CO_2 desublimation or sublimation.

In order to model CO_2 desublimation and sublimation using the LB method, the above physical parameters are converted to those in lattice units. For this purpose, dimensionless parameters are derived to act as the conversion criteria between the two systems of units. By introducing the characteristic length L, velocity U, temperature T_{ch} and density ρ_g, dimensionless parameters marked by asterisks are derived as

$$\left.\begin{gathered} \boldsymbol{x}^* = \frac{\boldsymbol{u}}{L}, \quad t^* = \frac{t}{L/U}, \quad \boldsymbol{u}^* = \frac{\boldsymbol{u}}{U}, \quad \rho^* = \frac{\rho}{\rho_g}, \quad p^* = \frac{p}{\rho_g U^2}, \\ T^* = \frac{T}{T_{ch}}, \quad m_r^* = \frac{m_r}{\rho_g U}, \\ h_r^* = \frac{h_r}{c_{p,g} T_{ch}}, \quad k_r^* = k_r U, \quad Re = \frac{LU}{\nu}, \quad Pe = \frac{LU}{D}, \\ Pr = \frac{\nu}{\alpha_g}, \quad \Delta T_s = \frac{T_f - T}{T_{ch}}. \end{gathered}\right\} \tag{2.15}$$

The subscript g refers to physical properties of the flue gas and T_f is the freezing temperature of CO_2. From such a dimensionless derivation, key characteristic numbers are obtained: the Reynolds number Re, the Péclet number Pe, the Prandtl number Pr and the subcooling degree ΔT_s. In LB simulations a match of these dimensionless variables ensures the same desublimation and sublimation characteristics between the lattice space and the real physical space.

3. Numerical method

The LB method is applied to solve the conservation equations (2.8)–(2.11) in two dimensions. Considering the porous structure of the packed bed, the multiple-relaxation-time (MRT) LB method is employed to avoid the unphysical dependence of permeability on viscosity at the pore scale (Pan, Luo & Miller 2006). To enforce the boundary conditions in (2.12)–(2.14) for CO_2 desublimation and sublimation, LB boundary schemes are developed. Furthermore, the volume-of-pixel (VOP) method is adopted to treat the evolution of solid CO_2 in (2.7) (Kang, Lichtner & Zhang 2006; Wang *et al.* 2019; Lei & Luo 2021).

3.1. *The MRT LB models*

Since the flue gas and the solid phases have different thermophysical properties, the energy conservation equation (2.11) is recast as

$$\partial_t T + \boldsymbol{\nabla} \cdot (T\boldsymbol{u}) = \boldsymbol{\nabla} \cdot (\alpha \boldsymbol{\nabla} T) + F_T, \tag{3.1}$$

with the source term F_T being

$$F_T = F_{T1} + F_{T2}, \quad F_{T1} = \frac{Q}{\rho c_p}, \quad F_{T2} = \frac{1}{\rho c_p}\boldsymbol{\nabla}\left(\rho c_p\right) \cdot (\alpha \boldsymbol{\nabla} T - T\boldsymbol{u}) - \frac{T}{\rho c_p}\partial_t\left(\rho c_p\right). \tag{3.2a–c}$$

More details on this derivation can be found in our earlier work (Lei, Wang & Luo 2021).

To solve the gas flow ((2.8)–(2.9)), species transport (2.10) and heat transfer (3.1), three sets of LB evolution equations are built as follows (Lei & Luo 2019; Lei *et al.* 2023):

$$f_i\left(\boldsymbol{x} + \boldsymbol{e}_i\delta_t, t + \delta_t\right) - f_i\left(\boldsymbol{x}, t\right) = -\left(\boldsymbol{M}^{-1}\boldsymbol{S}\boldsymbol{M}\right)_{ij}\left[f_j\left(\boldsymbol{x}, t\right) - f_j^{eq}\left(\boldsymbol{x}, t\right)\right], \tag{3.3}$$

$$g_i\left(\boldsymbol{x} + \boldsymbol{e}_i\delta_t, t + \delta_t\right) - g_i\left(\boldsymbol{x}, t\right) = -\left(\boldsymbol{M}^{-1}\boldsymbol{S}_y\boldsymbol{M}\right)_{ij}\left[g_j\left(\boldsymbol{x}, t\right) - g_j^{eq}\left(\boldsymbol{x}, t\right)\right], \tag{3.4}$$

$$h_i\left(\boldsymbol{x} + \boldsymbol{e}_i\delta_t, t + \delta_t\right) - h_i\left(\boldsymbol{x}, t\right) = -\left(\boldsymbol{M}^{-1}\boldsymbol{S}_t\boldsymbol{M}\right)_{ij}\left[h_j\left(\boldsymbol{x},\ t\right) - h_j^{eq}\left(\boldsymbol{x},\ t\right)\right] + \delta_t\bar{F}_{T,i} + \frac{\delta_t^2}{2}\frac{\partial \bar{F}_{T,i}}{\partial t}. \tag{3.5}$$

Here i and j are discrete directions. For fluid moving with the discrete velocity $\boldsymbol{e}_i$ at position $\boldsymbol{x}$ and time t, $f_i(\boldsymbol{x}, t)$, $g_i(\boldsymbol{x}, t)$ and $h_i(\boldsymbol{x}, t)$ are their distribution functions of the hydrodynamic, CO_2 mass fraction and temperature fields, respectively. Here f_i^{eq}, g_i^{eq} and h_i^{eq} are the equilibrium distribution functions; $\bar{F}_{T,i}$ is the distribution function for the thermal source term F_T; $\boldsymbol{S}$, $\boldsymbol{S}_y$ and $\boldsymbol{S}_t$ are the diagonal relaxation matrices, whereas $\boldsymbol{M}$ is the transformation matrix to map distribution functions from the physical space to the moment space. The time derivatives in (3.2*a–c*) ($\partial_t \rho c_p$) and (3.5) ($\partial_t \bar{F}_{T,i}$) are treated with a backward difference scheme.

At each time step, after the above evolutions, the macroscopic variables are calculated as

$$\rho_p = \sum_i f_i, \quad \rho_g \boldsymbol{u} = \sum_i \boldsymbol{e}_i f_i, \quad Y = \sum_i g_i, \quad T = \sum_i h_i. \tag{3.6a–d}$$

Here, ρ_p is a variable related to the gas pressure as $\rho_p = p/c_s^2$; $c_s = e/\sqrt{3}$ is the lattice sound speed and $e = \delta_x/\delta_t$ is the lattice speed; δ_x and δ_t denote the lattice spacing and time step, respectively.

3.2. *The LB boundary scheme for CO_2 desublimation and sublimation*

For the active gas–solid interface $I_{d,s}$ with CO_2 desublimation and sublimation, three boundary conditions (i.e. (2.12)–(2.14)) need to be addressed. First, the conjugate heat transfer in (2.14) is automatically realized by solving the energy conservation equation (3.1). Then, the no-slip velocity condition in (2.12) is achieved by the halfway bounce-back scheme. Finally, to implement the species mass conservation condition in (2.13), the CO_2

mass fraction gradient at the active interface $I_{d,s}$ is calculated based on the finite-difference scheme as (Zhang *et al.* 2012)

$$\boldsymbol{n}\cdot\nabla Y^{I_{d,s}} = \frac{Y^{g} - Y^{I_{d,s}}}{0.5\boldsymbol{n}\cdot\boldsymbol{e}_i\delta_x}, \tag{3.7}$$

where Y^g is the CO_2 mass fraction at the gas grid neighbouring the interface $I_{d,s}$. By inserting (3.7) into (2.13) and using the ideal gas law, the value of $Y^{I_{d,s}}$ is calculated as

$$Y^{I_d} = \frac{D\rho_g Y^l + 0.5\boldsymbol{n}\cdot\boldsymbol{e}_i\delta_x k_r p_e}{D\rho_g + 0.5\boldsymbol{n}\cdot\boldsymbol{e}_i\delta_x k_r p_0 T/T_0}, \tag{3.8}$$

$$Y^{I_s} = \frac{D\rho_g Y^l + 0.5\boldsymbol{n}\cdot\boldsymbol{e}_i\delta_x k_r A p_e}{D\rho_g + 0.5\boldsymbol{n}\cdot\boldsymbol{e}_i\delta_x k_r A p_0 T/T_0}. \tag{3.9}$$

In this way, the CO_2 mass fractions at the desublimation boundary I_d and the sublimation boundary I_s are obtained. Therefore, the mass conservation boundary condition in (2.13) can be re-expressed as (3.8)–(3.9), namely, a boundary with a given CO_2 mass fraction $Y^{I_{d,s}}$. The halfway bounce-back scheme is used to impose this boundary condition, with the unknown distribution functions at the gas grid $\boldsymbol{x}_g$ adjacent to $I_{d,s}$ being (Zhang *et al.* 2012)

$$g_{\bar{i}}\left(\boldsymbol{x}_g, t+\delta_t\right) = -g_i'\left(\boldsymbol{x}_g, t\right) + 2w_i Y^{I_{d,s}}. \tag{3.10}$$

Here, the superscript $'$ denotes the post-collision distribution function, $\bar{i}$ is the opposite direction of i as $\boldsymbol{e}_i = -\boldsymbol{e}_{\bar{i}}$ and $\boldsymbol{e}_i$ points to the solid phase zone. More details on the present MRT LB model and boundary treatments are provided in Appendices A and B.

3.3. *Evolution of solid CO_2*

With the desublimation and sublimation of CO_2, the evolution of a solid CO_2 structure at the pore scale is tracked by (2.7). In LB simulations this structure evolution is realized by the commonly used VOP method (Kang *et al.* 2006; Wang *et al.* 2019). Explicitly, a fine enough mesh is selected to cover the computational domain and each grid node (or pixel) is located at the centre of a control cell with size $1\times1\times1$ in lattice units. Each grid is assumed to represent a cell composed of a single material: solid grain cell, solid CO_2 cell or flue gas cell. Initially, the volume of solid CO_2 is set as $V_s = 1$ for solid CO_2 grids, $V_s = 0$ for gas grids and $V_s = 0$ for packing grain grids, respectively. As the desublimation and sublimation of CO_2 occurs, the value of V_s is calculated at each time step by

$$V_s\left(t+\delta_t\right) = V_s\left(t\right) + m_r a_r V_r/\rho_s. \tag{3.11}$$

With the desublimation of CO_2 (i.e. $m_r > 0$), the value of V_s increases with time. As V_s doubles at a solid CO_2 grid (i.e. $V_s = 2$) or increases to $V_s = 1$ in a grain grid, one of its neighbouring gas grids is converted into a solid CO_2 grid. The ratio of the growth probability between the nearest and the diagonal grids is $R_{dp} = 1:0.25$, which is consistent with the ratio of weight coefficients w_i (Lei *et al.* 2023). On the other hand, V_s decreases with the sublimation of CO_2 (i.e. $m_r < 0$). As V_s decreases to zero, the solid CO_2 grid is turned into a gas grid.

3.4. *Numerical procedure*

The developed MRT LB model for CO_2 desublimation and sublimation was programmed in the C language, following the algorithmic flowchart in figure 3. The main steps are as follows.

(i) Start the process and initialize the gas flow, temperature and CO_2 mass fraction fields.
(ii) Solve the flow field to update the gas velocity $\boldsymbol{u}$.
(iii) Simulate the heat and CO_2 transfer to obtain temperature T and CO_2 mass fraction Y.
(iv) Calculate the mass transfer rate m_r and classify three gas–solid boundaries as I_n, I_d and I_s.
(v) Implement CO_2 desublimation and sublimation at boundaries I_d and I_s, leading to changes in gaseous CO_2 mass fraction $Y^{I_{d,s}}$, solid CO_2 volume V_s and heat terms $Q_{d,s}$.
(vi) Track evolutions of solid CO_2 structure, bringing about changes in flow channels and thermophysical properties of updated grids.
(vii) Enforce boundary conditions at both external and internal boundaries.
(viii) Repeat (ii)–(vii) until the stop criterion is satisfied.

To enable parallel execution, the message passing interface library is utilized and the developed LB code is validated comprehensively. Appendix C is provided to elucidate model validation tests. Upon the validation of the developed LB code, pore-scale simulations are conducted to investigate CO_2 desublimation and sublimation on a single packing grain and in a packed bed, employing 640 and 1280 compute cores for the simulations of each configuration, respectively. In contrast to our prior investigation of CO_2 desublimation on an isothermal grain (Lei *et al.* 2023), the current study expands the scope to encompass both desublimation and sublimation of CO_2 within the context of CCC. The mathematical frameworks built here are augmented by incorporating new phase change processes ((2.1)–(2.2)) and modified mass transfer rates (2.3). These enhancements facilitate a comprehensive treatment of the multiphysics behind CCC, including the released desublimation heat Q_d and the absorbed sublimation heat Q_s, the dynamic boundaries pertinent to CO_2 desublimation I_d and sublimation I_s, and the generation and consumption of solid CO_2. Consequently, the boundary schemes and the evolution of solid CO_2 in the present LB model allow for a more detailed physical description of the phenomena compared with those in our previous research (Lei *et al.* 2023).

4. Results and discussion

For the cryogenic packed bed in figure 2, key geometrical parameters are set as: length $l_x = 124.8$ mm, width $l_y = 20.8$ mm, grain diameter $l_d = 10.0$ mm and porosity $\psi = 0.64$. From such a bed, a small-size domain encompassing a single grain is selected for single-grain simulations. The void volume fraction of this small-size domain equals the bed porosity ψ and the other geometrical parameters are $l_{sx} = 14.7$ mm and $l_{sy} = 14.7$ mm. Initially, packing grains are cooled to T_w for CO_2 desublimation and flow paths among grains are filled with N_2 at temperature T_w. The incompressible flue gas at the initial condition (T_0, Y_0, u_0, p_0) is fed in from the left inlet ($x = 0$) and the component CO_2 is desublimated on packing grains. The four external boundaries of the computational domain are set as follows: the flue gas at (T_0, Y_0, u_0, p_0) is fed in from the inlet, a fully

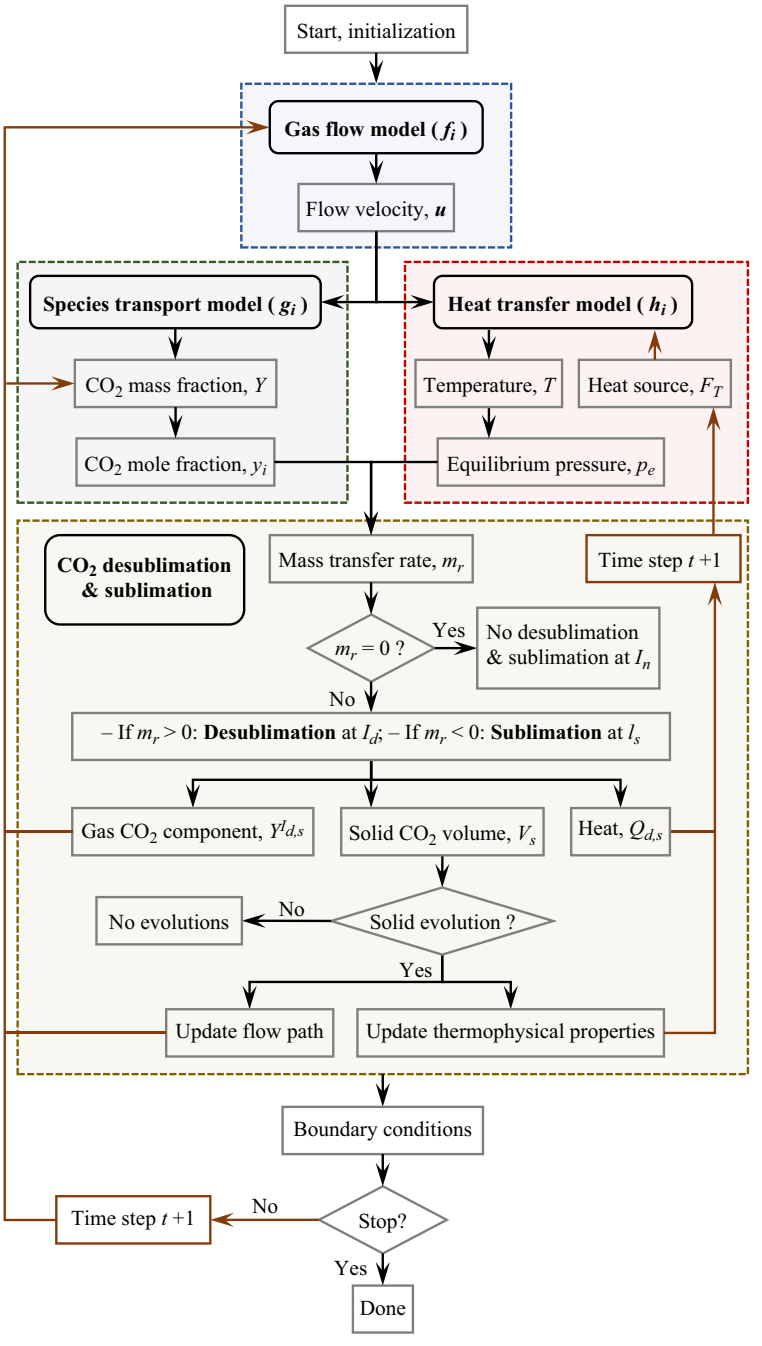

Figure 3. The schematic diagram of the overall numerical implementation.

developed flow is considered at the outlet, the periodic conditions are imposed at the bottom and top. More details of these boundaries are provided in Appendix B.

The desublimation parameters and thermophysical properties used in the following simulations are listed in table 1. These physical parameters are converted into lattice units by matching the dimensionless parameters in (2.15), where characteristic parameters are

Symbol	Definition	Value
l_x	Length of packed bed	124.8 mm
l_y	Width of packed bed	20.8 mm
l_d	Packing grain diameter	10.0 mm
ψ	Bed porosity	0.64
l_{sx}	Length of single-grain domain	14.7 mm
l_{sy}	Width of single-grain domain	14.7 mm
k_r	Mass desublimation rate constant	10^{-6} s m^{-1}
h_r	Enthalpy change of desublimation	5.682×10^5 J kg^{-1}
u_0	Flue gas feed rate	$[0.122, 6.10] \times 10^{-2}$ m s^{-1}
T_w	Initial bed temperature	[80, 180] K
T_0	Flue gas temperature	293 K
p_0	Flue gas pressure	0.1 MPa
ν	Flue gas kinematic viscosity	7.12×10^{-6} m^2 s^{-1}
Y_0	CO_2 mass fraction	1.0
D	CO_2 diffusion coefficient	1.63×10^{-5} m^2 s^{-1}
T_f	Freezing point of CO_2 at p_0	194 K
ρ_g	Flue gas density	1.46 kg m^{-3}
$c_{p,g}$	Flue gas specific heat capacity	0.846 kJ kgK^{-1}
α_g	Flue gas thermal diffusivity	5.02×10^{-6} m^2 s^{-1}
ρ_c	Packing grain density	2.55×10^3 kg m^{-3}
$c_{p,c}$	Packing grain specific heat capacity	0.841 kJ kgK^{-1}
α_c	Packing grain thermal diffusivity	3.74×10^{-7} m^2 s^{-1}
ρ_s	Solid CO_2 density	1.56×10^3 kg m^{-3}
$c_{p,s}$	Solid CO_2 specific heat capacity	0.967 kJ kgK^{-1}
α_s	Solid CO_2 thermal diffusivity	4.64×10^{-7} m^2 s^{-1}

Table 1. Physical properties for simulations of CO_2 desublimation and sublimation during CCC.

selected as

$$L = l_y, \quad U = u_0, \quad \rho_{ch} = \rho_g, \quad T_{ch} = T_0. \tag{4.1a–d}$$

Prior studies have noted the importance of the gas feed rate and initial bed temperature to the carbon capture performance of CCC. Therefore, u_0 and T_w are varied to change the operating conditions, covering u_0 from 1.22×10^{-3} m s^{-1} to 6.10×10^{-2} m s^{-1} and T_w from 80 K to 180 K. These two parameters are characterized by the Péclet number Pe and the subcooling degree of bed $\Delta T_s = (T_f - T_w)/T_0$, which lie in ranges of [1.55, 77.84] and [0.049, 0.389], respectively. Values of these two parameters are listed in table 2 in Appendix D.

To ensure the numerical solution is grid independent, grid convergence tests were carried out first. Two meshes of size 5400×900 and 640×640, with a lattice resolution 0.023 mm, are selected to describe the cryogenic packed bed and the small-size domain in figure 2. Details about the grid convergence tests are provided in the supplementary material. Since both the capture and recovery steps of CCC are considered, each simulation test is continued until all the desublimated CO_2 is sublimated to gaseous CO_2 at the time instant t_e, which is termed as the operating time.

4.1. *CO_2 desublimation and sublimation on a single packing grain*

The initial objective of this study is to identify the CO_2 desublimation and sublimation properties on a single packing grain. A test with the subcooling degree $\Delta T_s = 0.185$

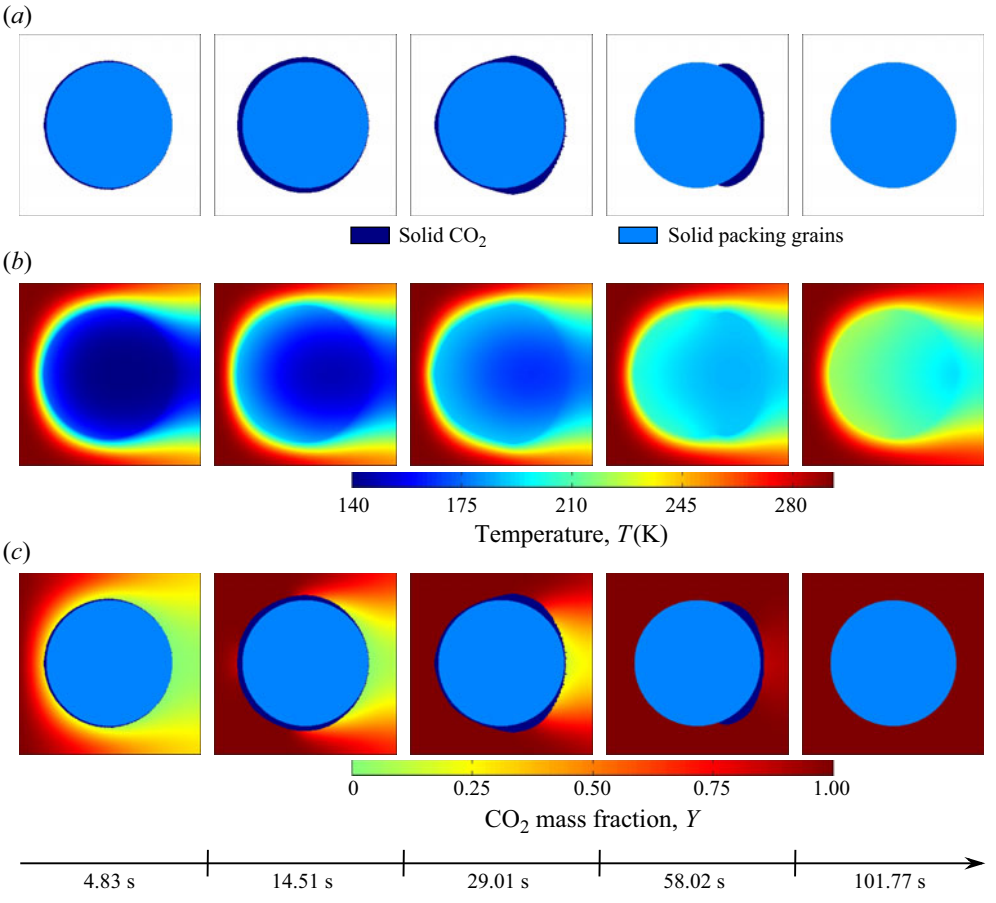

Figure 4. The CO_2 desublimation and sublimation properties on a single packing grain with the subcooling degree $\Delta T_s = 0.185$ and the Péclet number $Pe = 15.57$. Contours of (*a*) solid CO_2, (*b*) temperature (T) and (*c*) CO_2 mass fraction (Y) at five time instants $t = 4.83$, 14.51, 29.01, 58.02, 101.77 s.

and the Péclet number $Pe = 15.57$ is simulated. The obtained distributions of solid CO_2, temperature T and CO_2 mass fraction Y at five time instants are provided in figure 4.

In the early stage (figure 4 at $t = 4.83$, 14.51 s), the injected flue gas is cooled by the grain and its component CO_2 is desublimated to generate SCL on the grain surface. Meanwhile, the incoming warm flue gas and the heat Q_d released from CO_2 desublimation raise the temperature of the packing grain, which gradually brings about the sublimation of the previously generated SCL (figure 4 at $t = 29.01$ s). Following the continuous increase in grain temperature, the desublimation strength of CO_2 on the grain surface starts to decrease. As a result, the evident sublimation of SCL is observed compared with its generation (figure 4 at $t = 58.02$ s). Finally, the grain becomes warm and SCL is completely sublimated to gaseous CO_2 at $t_e = 101.77$ s, signaling the cessation of both CO_2 desublimation and sublimation.

Given the vital role of the captured SCL in assessing the performance of CCC, the volume fraction of solid CO_2 (ϕ_c) on the packing grain is quantified by

$$\phi_c = \frac{1}{l_x l_y} \int_0^{l_x} \int_0^{l_y} V_s\,(x, y)\ \mathrm{d}y\,\mathrm{d}x. \tag{4.2}$$

The calculated ϕ_c is recorded versus time in figure 5(a), whose behaviour is explained with the help of the averaged temperature ($\bar{T}_a$) and overall mass transfer rates via desublimation and sublimation (m_r^*) in figure 5(b–d). Here $\bar{T}_a$ is defined as the averaged temperature for the active gas–solid interface $I_{d,s}$, where CO_2 desublimation and sublimation take place:

$$\bar{T}_a = \frac{1}{I_{d,s}} \sum_{I_{d,s}} T\,(x, y)\,. \tag{4.3}$$

The overall mass transfer rates are calculated as

$$\left.\begin{aligned} m_{rd}^* = \frac{1}{\rho_g u_0} \sum_{I_d} m_r\,(x, y)\,, \quad m_{rs}^* = -\frac{1}{\rho_g u_0} \sum_{I_s} m_r\,(x, y)\,, \\ m_r^* = \frac{1}{\rho_g u_0} \sum_{I_{d,s}} m_r\,(x, y) = m_{rd}^* + (-m_{rs}^*). \end{aligned}\right\} \tag{4.4}$$

Here, m_{rd}^* and m_{rs}^* represent the mass transfer rates through desublimation at I_d and sublimation at I_s, respectively; m_r^* stands for the combined mass transfer rate by both desublimation and sublimation at $I_{d,s}$.

Initially, ϕ_c in figure 5(a) increases with time due to the stronger desublimation rate compared with the sublimation rate (i.e. $m_r^* > 0$ in figure 5c). The growth rate of ϕ_c is observed to decrease over time. As shown in figure 5(b–d), this is driven by the fact that the ascending $\bar{T}_a$ decelerates desublimation (m_{rd}^*) while accelerating sublimation (m_{rs}^*). Subsequently, the desublimation rate gradually drops to an equilibrium level with the sublimation rate at t_m (i.e. $m_r^* = 0$), where ϕ_c reaches a peak value ϕ_{cm}. Scalar distributions at this peak point t_m are shown in figure 5(e). After t_m, ϕ_c decreases until it reaches zero at $t_e = 101.77$ s, wherein the desublimation rate decreases steadily and becomes weaker than the sublimation rate (i.e. $m_r^* < 0$). The decrease in ϕ_c experiences an inflection point at t_i, after which the drop rate of ϕ_c slows down. This is because the SCL on the front part of the grain is completely sublimated at t_i, leading to the diminished sublimation rate. For illustration, figure 5(a) plots the temporal evolutions of ϕ_c for the front and back grain areas, and figure 5(f) provides the scalar distributions at t_i. Besides, the warm gas stream and CO_2 desublimation contribute to raising $\bar{T}_a$ towards an equilibrium value of approximately 189.3 K, which is in line with experimental findings (Tuinier *et al.* 2010, 2011*b*). Taken together, these quantitative analyses corroborate the above qualitative observations in figure 4 and also provide insights into the CO_2 desublimation and sublimation processes.

4.2. *Effects of Δt_s and Pe in the single-grain case*

In the single-grain case, after the discussion of general CO_2 desublimation and sublimation properties, a parametric study is set out to explore the impact of subcooling degree ΔT_s and Péclet number Pe on the carbon capture performance of the cold grain. The CO_2 desublimation and sublimation processes are simulated at Péclet numbers $Pe \in [1.55, 46.70]$, and each Pe contains a subsection of subcooling degrees $\Delta T_s \in [0.049,\ 0.389]$. From the above discussions on CO_2 desublimation and sublimation properties in § 4.1, two important metrics stand out to quantify the carbon capture performance of the grain, namely, the maximum volume fraction of solid CO_2 captured by the packing grain (ϕ_{cm}) and the operating time of the CO_2 desublimation and sublimation

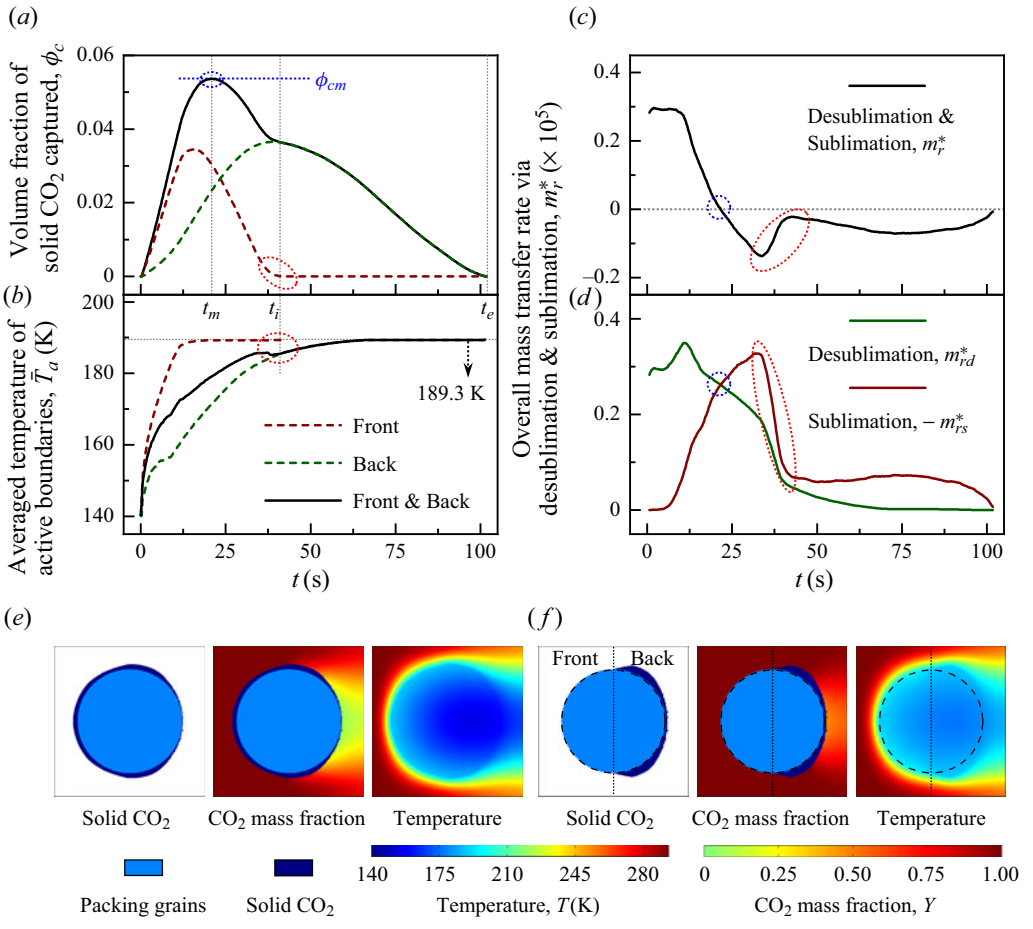

Figure 5. Analyses of CO_2 desublimation and sublimation on a single packing grain with the subcooling degree $\Delta T_s = 0.185$ and the Péclet number $Pe = 15.57$. Temporal evolutions of (*a*) volume fraction of the solid CO_2 captured (ϕ_c), (*b*) averaged temperature of active boundaries ($\bar{T}_a$) and (*c*,*d*) overall mass transfer rate via desublimation and sublimation (m_r^*, m_{rd}^* and m_{rs}^*). Contours of solid CO_2, temperature (T) and CO_2 mass fraction (Y) at (*e*) peak point t_m and (*f*) inflection point t_i.

processes (t_e). Based on these two metrics, the CO_2 capture rate (v_c) is calculated as

$$v_c = \frac{\phi_{cm}}{t_e}. \tag{4.5}$$

A grain with a larger v_c demonstrates a higher efficiency in capturing the CO_2 component, making it desirable.

Figure 6 depicts values of (ϕ_{cm}, t_e, v_c) for a wide range of ΔT_s and Pe, where each dot represents a simulation test at a given operating condition (ΔT_s, Pe). For a fixed Pe, effects of ΔT_s on the CO_2 capture performance of the grain share a similar trend: the successive rise in ΔT_s introduces the continuous increase in both t_e and ϕ_{cm}. For example, as ΔT_s varies from 0.049 to 0.389 at $Pe = 15.57$, ϕ_{cm} increases from 0.005 to 0.138 and t_e grows from 48.59 s to 150.84 s. As supported by figure 7(*a*), a possible explanation is that a packing grain with a higher ΔT_s holds a lower temperature $\bar{T}_p$. Under the fixed gas feed rate condition (i.e. constant Pe), the convective heat transfer strength is similar and, thus,

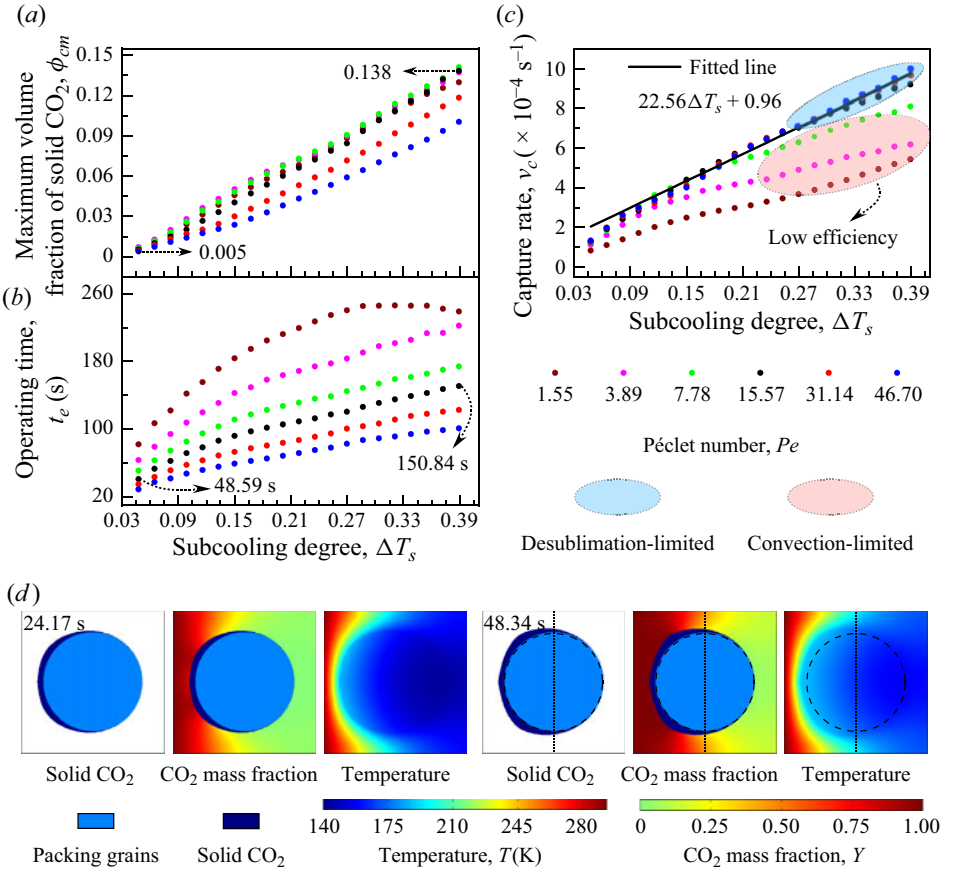

Figure 6. Analyses of CO_2 capture performance in single-grain tests with subcooling degrees $\Delta T_s \in [0.049, 0.389]$ and Péclet numbers $Pe = 1.55, 3.89, 7.78, 15.57, 31.14, 46.70$. (*a*) The maximum volume fraction of solid CO_2 captured by the grain (ϕ_{cm}). (*b*) The operating time for CO_2 desublimation and sublimation (t_e). (*c*) The CO_2 capture rate (v_c). (*d*) Contours of solid CO_2, temperature (T) and CO_2 mass fraction (Y) in a convection-limited test with $\Delta T_s = 0.185$ and $Pe = 1.55$ at two time instants $t = 24.17, 48.34$ s.

a colder grain requires a lengthier duration (t_e) for the incoming warm flue gas to heat it up. This subsequently produces an increased amount of solid CO_2 captured (ϕ_{cm}). On the other hand, v_c in figure 6(*c*) is seen to increase with the ascending ΔT_s, indicating that a colder packing grain is beneficial to improving the CO_2 capture performance of the grain. Meanwhile, based on the value of Pe, two distinct regimes arise from the comparison of v_c evolutions in response to changes in Pe and ΔT_s.

First, in large-Pe tests (e.g. $Pe > 7.8$ at $\Delta T_s = 0.185$), the increasing ΔT_s accelerates v_c, while Pe has minimal or no effects on it. Accordingly, a correlation is fitted as $v_c = 22.56\Delta T_s - 0.76$. As shown in figure 7(*a*,*b*), for a fixed Pe in this regime, the larger ΔT_s brings about the colder packing grain ($\bar{T}_p$) and the faster mass transfer rate (m_r^*), introducing the accelerated CO_2 capture rate v_c. On the other hand, the negligible impact of increasing Pe on v_c can be explained by effects of convection between the warm gas stream and solid phases. The rapid convective gas flow augments the CO_2 delivery and amplifies the CO_2 desublimation rate. At the same time, however, the fast convective heat transfer rapidly heats up the grain and consequently slows down the desublimation of CO_2.

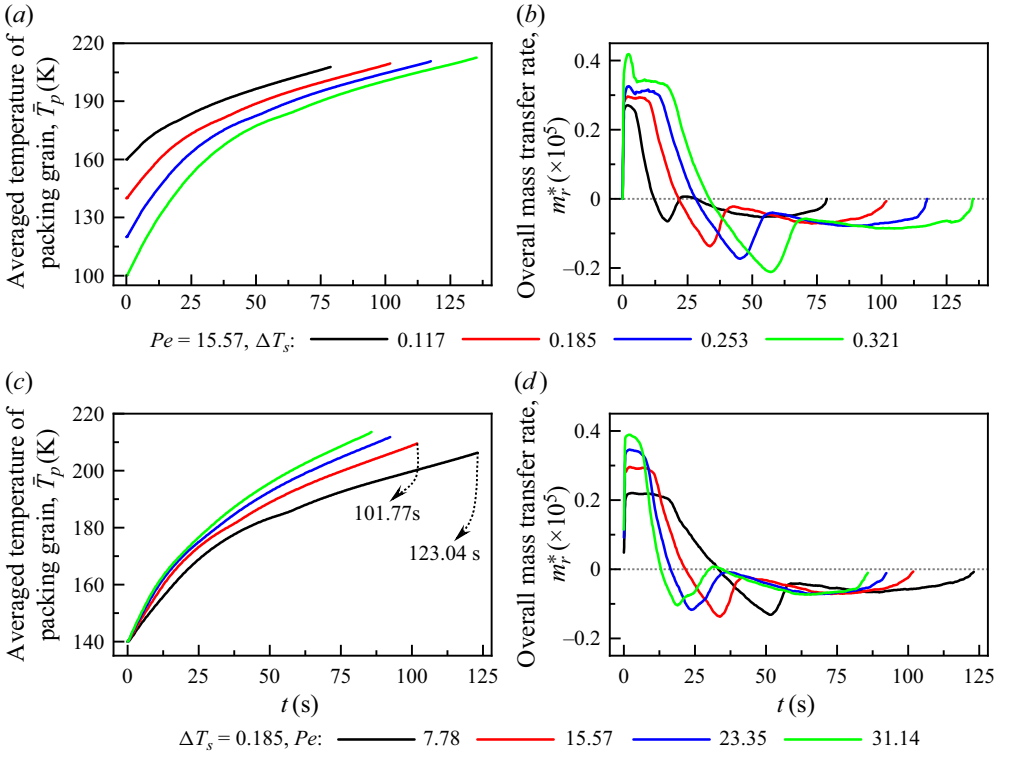

Figure 7. Analyses of CO_2 capture performance in single-grain tests with subcooling degrees $\Delta T_s = 0.117, 0.185, 0.253, 0.321$ and Péclet numbers $Pe = 7.78, 15.57, 23.35, 31.14$. Temporal evolutions of (*a*,*c*) averaged temperature of the packing grain ($\bar{T}_p$) and (*b*,*d*) overall mass transfer rate via desublimation and sublimation (m_r^*).

Figure 7(*c*,*d*) is presented to corroborate the aforementioned effects of *Pe*. Following the growing *Pe* in this regime, the CO_2 supply is abundant and m_r^* is amplified at first ($t < 6$ s in figure 7*d*). After a short period, the ascending *Pe* intensifies the convective heat transfer, yielding a significant increase in $\bar{T}_p$ and a rapid slowdown in m_r^* ($t > 6$ s in figure 7*c*,*d*). As a result, the high *Pe* leads to a reduction in both t_e and ϕ_{cm} (figure 6*a*,*b*). Since t_e and ϕ_{cm} exhibit a similar decrease rate, v_c is barely or not affected by *Pe*. Considering that v_c is primarily influenced by ΔT_s (or desublimation) rather than *Pe*, the CO_2 desublimation and sublimation processes in the large-*Pe* range are denoted as the desublimation-limited (or subcooling-limited) regime.

Second, as *Pe* decreases to a rather small value (e.g. $Pe < 7.8$ at $\Delta T_s = 0.185$), the increase in ΔT_s leads to the growing ϕ_{cm}, t_e and v_c, which is in line with the above desublimation-limited regime. However, the decline in *Pe* induces a growth in t_e but a slight variation in ϕ_{cm}, giving rise to the diminished v_c. Therefore, both ΔT_s and *Pe* play roles in determining v_c, making v_c deviate from the correlation $v_c = 22.56\Delta T_s - 0.76$. This inconsistency from the desublimation-limited regime stems from the weak convection under small *Pe*. It is clear from figure 7(*c*,*d*) that the weak convective heat transfer extends the time period for heating up the packing grain, resulting in the prolonged t_e. For example, the decreased *Pe* from 15.57 to 7.78 leads to the augmented t_e from 101.77 s to 123.04 s. In addition, the inadequate CO_2 supply via weak gas convection, along with the fixed ΔT_s, results in the unchanged or even marginally diminished ϕ_{cm}. The combination of

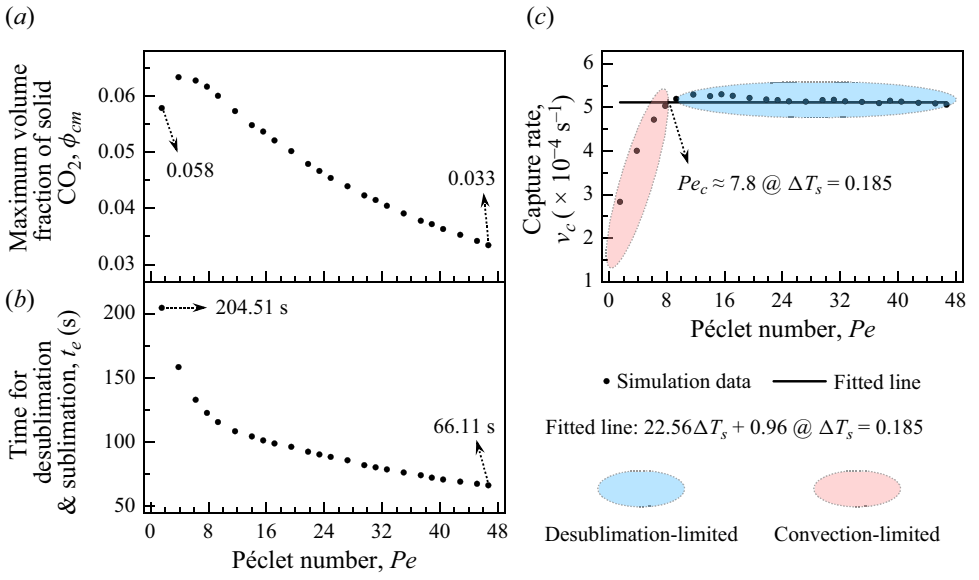

Figure 8. Analyses of CO_2 capture performance in single-grain tests with the subcooling degrees $\Delta T_s = 0.185$ and the Péclet numbers $Pe \in [1.55, 46.70]$. (*a*) The maximum volume fraction of solid CO_2 (ϕ_{cm}) captured by the grain. (*b*) The operating time for CO_2 desublimation and sublimation (t_e). (*c*) The CO_2 capture rate (v_c).

these two factors is responsible for the obvious departure of v_c from the correlation. These small-*Pe* tests are classified as the convection-limited regime due to the weak convection. As an example, figure 6(*d*) provides scalar distributions in a convection-limited test with $\Delta T_s = 0.185$ and $Pe = 1.55$. The insufficient CO_2 supply via weak convection is illustrated clearly by contours of the CO_2 mass fraction.

To directly demonstrate impacts of *Pe* on the CO_2 capture performance of the cold grain, simulation results for $Pe \in [1.55, 46.70]$ and $\Delta T_s = 0.185$ are presented in figure 8. With the growing *Pe*, there is an obvious drop in both ϕ_{cm} and t_e, while v_c initially experiences a sharp increase and then stabilizes after reaching the threshold of $Pe_c \approx 7.8$ (at $\Delta T_s = 0.185$). Accordingly, the CO_2 desublimation and sublimation processes shift from the convection-limited regime to the desublimation-limited regime. These tendencies corroborate findings in figure 6, which are driven by changes in the relative strength between convection and desublimation.

Finally, a comprehensive map of the simulated v_c is plotted against $\Delta T_s \in [0.049, 0.389]$ and $Pe \in [1.55, 46.70]$ in figure 9. For comparison, the calculated v_{cr} via the correlation $v_c = 22.56\Delta T_s - 0.76$ is presented as a grey surface. Here v_c aligns closely with v_{cr} in the large-*Pe* region but exhibits notable deviations in the small-*Pe* space. Thereby, distributions of the convection-limited (I) and desublimation-limited (II) regimes are obtained in the ΔT_s–*Pe* parameter space (figure 10). The boundary line between the two regimes is established (i.e. solid white line in figure 9 and grey dash line in figure 10), with threshold values (ΔT_{sc}, Pe_c) situated upon this boundary. As the ΔT_s (or *Pe*) increases, there is a consequent growth in the threshold value of Pe_c (or ΔT_{sc}). This relationship reflects that the augmented convection strength is necessary to counterbalance the increased desublimation rate. According to the regime diagram, it is essential that ΔT_s stays below ΔT_{sc} and *Pe* exceeds Pe_c in order to ensure the desublimation-limited regime and prevent weak convection limitations. Note that, the continuous increase in *Pe* beyond Pe_c is unnecessary as it no longer accelerates v_c. Although a large ΔT_s helps accelerate v_c,

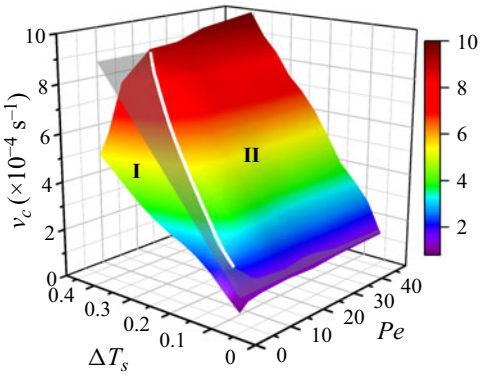

Figure 9. Analyses of the CO_2 capture rate v_c in single-grain tests with subcooling degrees $\Delta T_s \in [0.049, 0.389]$ and Péclet numbers $Pe \in [1.55, 46.70]$. The grey surface represents the correlation $v_c = 22.56\Delta T_s - 0.76$. The white solid line shows the boundary between the convection-limited (I) and desublimation-limited (II) regimes.

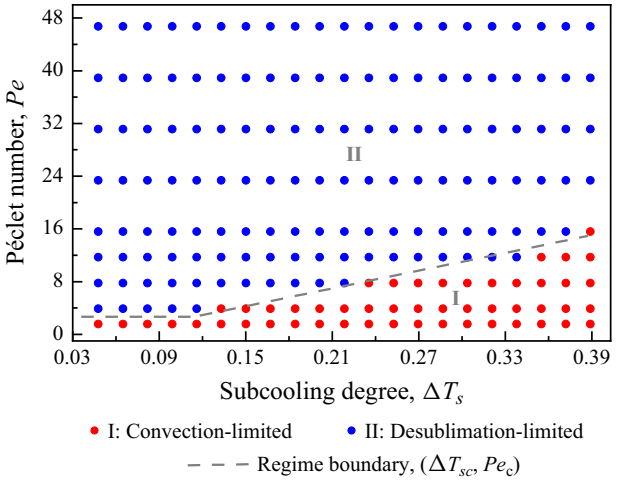

Figure 10. Analyses of CO_2 capture performance in single-grain tests with subcooling degrees $\Delta T_s \in [0.049, 0.389]$ and Péclet numbers $Pe \in [1.55, 46.70]$. Simulation data points are plotted against ΔT_s and Pe. The grey dashed line divides the plane into the convection-limited (I) and desublimation-limited (II) regimes.

ΔT_s should be increased with caution because it has the potential to significantly boost the cooling duty. This aspect is beyond the scope of the present work and will be considered in our future work. In general, the regime diagram can provide guidance on how to select operation conditions for an optimal CCC system.

The thematically aligned research we conducted earlier explored CO_2 desublimation on an isothermal grain during the capture of CCC (Lei *et al.* 2023). In contrast, this work extends to investigate both CO_2 desublimation and sublimation on a non-isothermal grain, encompassing the capture and recovery of CCC. These considerations make the present study incorporate a more comprehensive thermal interaction between grains and flow, leading to significantly distinct results that are more realistic in an actual CCC process. Some key differences are summarized as follows. (1) The diffusion-controlled and join-controlled regimes are no longer as distinct as they were predicted in the previous study (Lei *et al.* 2023), because the increase in the grain temperature diminishes the

desublimation rate over time. (2) The previous study predicted that the solid CO_2 captured (ϕ_{cm}) continued to increase with Pe, while the present model shows that an increase in Pe results in a decrease in ϕ_{cm} due to the diminished desublimation rate. (3) The previous study demonstrated an unrealistically high desublimation rate as ΔT_s increases. This results in the formation of cluster-like SCLs with highly porous structures, leading to a reduced desublimation duration and ϕ_{cm}. By contrast, the present study correctly predicts that the ascending ΔT_s results in the growing ϕ_{cm} and the extended desublimation duration. (4) The sublimation of SCL and the CO_2 capture rate v_c are newly analysed here, producing new and valuable insights into CO_2 desublimation and sublimation during CCC. Therefore, the present study provides more realistic and valuable insights into the CCC process and allows an improved understanding compared with our previous approach (Lei *et al.* 2023). In the following subsection, CO_2 desublimation and sublimation in a cryogenic packed bed are discussed.

4.3. *The CO_2 desublimation and sublimation in a packed bed*

In the packed-bed case, simulation tests for a wide range of subcooling degrees ΔT_s and Péclet numbers Pe are performed, which successfully reproduce CO_2 desublimation and sublimation properties during the capture and recovery steps of CCC. For illustration, figure 11(*a*,*b*) depicts numerical results for the test with $\Delta T_s = 0.185$ and $Pe = 15.57$, including contours of solid CO_2 and temperature distributions at five time instants. When feeding the warm flue gas to the packed bed, the flue gas is cooled until its component CO_2 starts to desublimate and generates an SCL on the packing grains. As time goes on, the SCL grows on the grains and forms a desublimation front (l_d), which expands toward the outlet. In the meantime, under effects of the incoming warm flue gas and the exothermic CO_2 desublimation process, packing grains close to the inlet are significantly heated from T_w to T_0. Owing to such a rise in temperature, the previously formed SCL is sublimated and a sublimation front (l_s) develops. Following l_d, l_s also progresses outwards but at a smaller velocity. In the packed bed, grains from l_s to l_d are coated by solid CO_2 and, thus, they are denoted as the SCL area.

For quantification, vertically averaged scalars ($\bar{\zeta}_x$) are introduced as

$$\bar{\zeta}_x = \frac{1}{l_y}\int_0^{l_y} \zeta\,(x, y)\ \mathrm{d}y, \quad \text{with } \zeta = V_s, T, Y. \tag{4.6}$$

Figure 11(*c*,*d*) presents the vertically averaged volume fraction of solid CO_2 (ϕ_{cx}) and temperature ($\bar{T}_x$) at two time instants. The calculated profiles of $\bar{T}_x$ for both grains (dashed lines) and gas (solid lines) exhibit a declining trend from the inlet to the outlet. On the other hand, ignoring fluctuations introduced by variations in the grain surface along the x direction, curves of ϕ_{cx} change non-monotonically from the inlet to the outlet. For instance, at 86.74 s, starting from the inlet ϕ_{cx} remains zero at first, then it rises to a maximum value, subsequently it decreases back to zero and finally it remains constant until the outlet. From each profile of ϕ_{cx}, the desublimation and sublimation fronts are identified as the two positions with $\phi_{cx} = 0.01$. The region between these two fronts corresponds to the SCL area. From the comparison of ϕ_{cx} profiles at 86.74 s and 322.17 s, it is evident that the SCL area together with the two fronts propagate outwards. These findings quantitatively support the observations in figure 11(*a*,*b*).

As l_d arrives at the bed exit, the component CO_2 starts to break through the packed bed and the outgoing CO_2 mass fraction gradually grows to the inlet value, i.e. $Y(l_x) = Y_0$. This phenomenon is termed the operational saturation and the CCC system is thus switched to

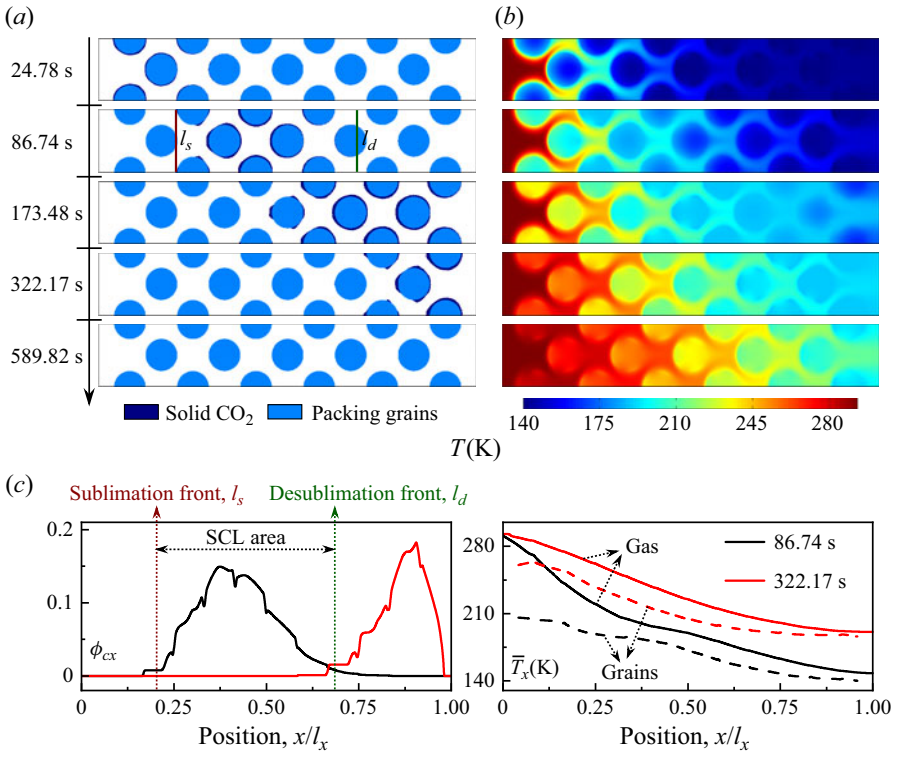

Figure 11. The CO_2 desublimation and sublimation properties in a packed bed with the subcooling degree $\Delta T_s = 0.185$ and the Péclet number $Pe = 15.57$. Contours of (*a*) solid CO_2 and (*b*) temperature (T) at five time instants $t = 24.78$, 86.74, 173.48, 322.17, 589.82 s. Vertically averaged (*c*) volume fraction of solid CO_2 (ϕ_{cx}) and temperature ($\bar{T}_x$) at two time instants $t = 86.74$, 322.17 s.

the recovery step. To clarify the saturation condition of the packed bed, figure 12 displays distributions of CO_2 mass fraction (Y) and profiles of the vertically averaged values ($\bar{Y}_x$) at three time instants. At the early stage (i.e. $t = 39.57$ s), packing grains are cold enough to fully capture the injected CO_2. Over time, grains are gradually heated by the incoming warm flue gas and the exothermic desublimation, and thus, the injected CO_2 passes warm grains and moves toward the exit. With the continuous rise in grain temperature, part of the injected CO_2 starts to leave the packed bed without desublimation (i.e. $t = 105.96$ s). The outlet CO_2 mass fraction progressively increases to a critical value (i.e. 10 % in this study), indicating that the bed reaches the saturation point $t_{sat} = 136.34$ s. After t_{sat}, the injected CO_2 is less efficiently captured and the CCC system enters the recovery step to collect the captured SCL. To quantify t_{sat}, profiles of $\bar{Y}_x$ are utilized to define the saturation front (l_{sat}) as the position with $\bar{Y}_x = 0.1$. Saturation point t_{sat} is then determined as the time instant when l_{sat} moves to the outlet (i.e. $t_{sat} = 136.34$ s in figure 12*b*).

Following the same procedure as in the single-grain case, temporal evolutions of the solid CO_2 volume fraction (ϕ_c) and the mass transfer rate (m_r^*) are calculated and plotted in figure 13 to quantify the CO_2 capture performance of the packed bed. Initially, the curve of ϕ_c experiences a sharp increase. This is because the packing grains are sufficiently cold and the CO_2 desublimation dominates the system. However, as grains are heated by the incoming warm gas and the released heat from desublimation Q_d, the mass transfer rate m_r^* drops to be negative. Consequently, the CO_2 sublimation controls the system and ϕ_c

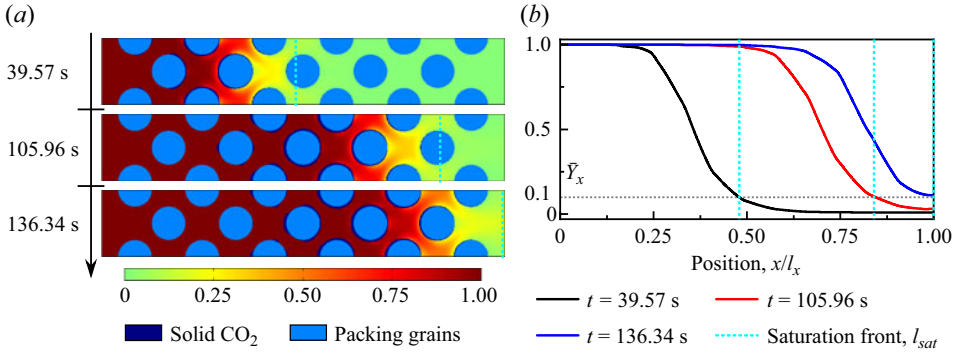

Figure 12. The CO_2 desublimation and sublimation properties in a packed bed with the subcooling degree $\Delta T_s = 0.185$ and the Péclet number $Pe = 15.57$. (*a*) Contours of CO_2 mass fraction (Y) and (*b*) vertically averaged CO_2 mass fraction ($\bar{Y}_x$) at three time instants $t = 39.57$, 105.96, 136.34 s.

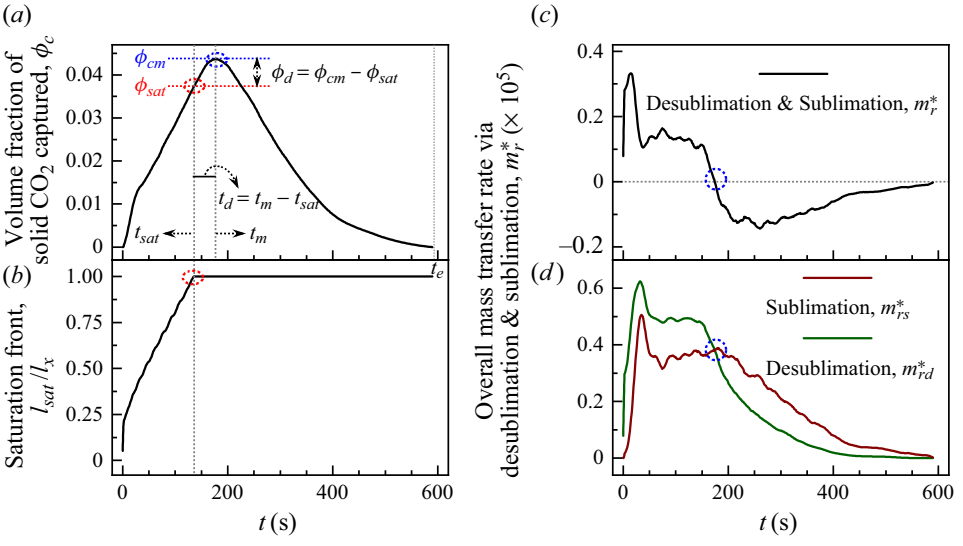

Figure 13. Analyses of CO_2 desublimation and sublimation in a packed bed with the subcooling degree $\Delta T_s = 0.185$ and the Péclet number $Pe = 15.57$. Temporal evolutions of (*a*) volume fraction of the solid CO_2 captured (ϕ_c), (*b*) position of the saturation front (l_{sat}) and (*c*,*d*) overall mass transfer rate via desublimation and sublimation (m_r^*, m_{rd}^* and m_{rs}^*).

starts to decrease until all the captured SCL is recovered at t_e. From this nonlinear profile of ϕ_c, the maximum solid CO_2 capture capacity of the packed bed is determined as ϕ_{cm} at t_m. The non-monotonic variation of ϕ_c aligns with that observed in the single-grain case in figure 5. In contrast, no inflection point is detected during the decreasing stage of ϕ_c here. This stems from the fact that the multiple packing grains help to average out the temperature difference between the front and back areas of each single grain.

For the operation of CCC in a packed bed, a key issue is the timely detection of the operational saturation point t_{sat}, at which the system should initiate the recovery step to gather the captured SCL. Otherwise, any delayed actions could result in detrimental consequences, such as CCC malfunction and flue gas breakthrough. For this purpose, the position of the saturation front (l_{sat}) is identified based on the vertically averaged CO_2 mass

fraction ($\bar{Y}_x$) and set out as a function of time in figure 13(*b*). There is a clear ascending trend in the temporal evolution of l_{sat} from the inlet ($l_{sat} = 0$) to the outlet ($l_{sat} = l_x$), which corroborates the outward movement of l_{sat} in figure 12. As marked by the red dash circle in figure 13(*b*), t_{sat} is quantitatively identified as the earliest time instant when l_{sat} advances to the outlet. One unexpected finding is that t_{sat} is earlier than t_m. During the operation of CCC, however, the system is desired to start the recovery of the SCL at t_m, so as to capture the maximum amount of CO_2. To quantify the performance degradation, two metrics associated with the time delay are defined. One is the delayed time period, $t_d = t_m - t_{sat}$, and the other one is the capacity loss

$$\eta_d = \frac{\phi_m - \phi_{sat}}{\phi_m}. \tag{4.7}$$

It is apparent that, as t_d and η_d approach zero, the carbon capture performance of the packed bed is optimal.

These numerically obtained CO_2 desublimation and sublimation properties in a packed bed accord closely with experimental observations during the capture and recovery steps (Tuinier *et al.* 2010, 2011*b*; Ali *et al.* 2014). Moreover, the detailed spatio-temporal evolution of scalar distributions and quantitative analyses, which are difficult to obtain from experiments, contribute to a better understanding of CCC. After that, parametric analyses are set out to elucidate the key operating factors. Compared with the single-grain case, the same range of $\Delta T_s \in [0.049, 0.389]$ is considered, while the range of Pe is extended to be $[6.23, 77.84]$ due to the resistance of multiple grains. In addition, the porous structure of the packed bed is expected to impact its flow channels and CO_2 capture performance. Therefore, the following packed-bed tests aim to examine effects of the gas velocity, bed temperature and bed structure.

4.4. *Effects of Δt_s and Pe in the packed-bed case*

From the above CO_2 desublimation and sublimation properties, four key metrics emerge for evaluating the CO_2 capture performance of the packed bed, including the maximum volume fraction of solid CO_2 captured (ϕ_{cm}), the operating time of CO_2 desublimation and sublimation (t_e), the CO_2 capture capacity loss due to the delay between the maximum point and the saturation point (η_d), and the CO_2 capture rate (v_c). These four metrics are calculated and analysed for packed-bed tests with varying ΔT_s and Pe.

Figure 14 compares values of metrics (ϕ_{cm}, t_e, η_d, v_c) for tests with $\Delta T_s \in [0.049, 0.389]$ and $Pe = 15.57, 31.14, 46.70, 62.27, 77.84$. As ΔT_s increases at a fixed Pe, the results follow a similar trend. On the one hand, a rise in ΔT_s increases ϕ_{cm} and t_e (figure 14*a*,*b*). As explained in the single-grain case, this stems from the lower temperature in grains and the enhanced desublimation intensity (m_r). On the other hand, the ascending ΔT_s yields the growing v_c but at a diminished growth rate (figure 14*d*). From comparisons of results at different Pe numbers, it is evident that the large Pe (or fast gas convection) amplifies v_c. Incorporating impacts of both ΔT_s and Pe, a correlation is established to fit the simulation data as $v_c = (0.02Pe - 0.19)\ln(\Delta T_s - 0.024) + (0.083Pe - 0.37)$. Therefore, v_c is determined by both ΔT_s and Pe in the packed-bed case, suggesting all the packed-bed tests operate in the convection-limited regime. Unlike the single-grain case, no linear correlation between ΔT_s and v_c appears and the desublimation-limited regime is not identified. This difference stems from the presence of multiple grains in the packed bed, which lead to the insufficient CO_2 supply and the convection-limited mechanism.

Figure 14(*c*) displays results of η_d, a parameter absent in the single-grain case. An ascending ΔT_s is found to yield a consistent drop in η_d (or diminished CO_2 capture

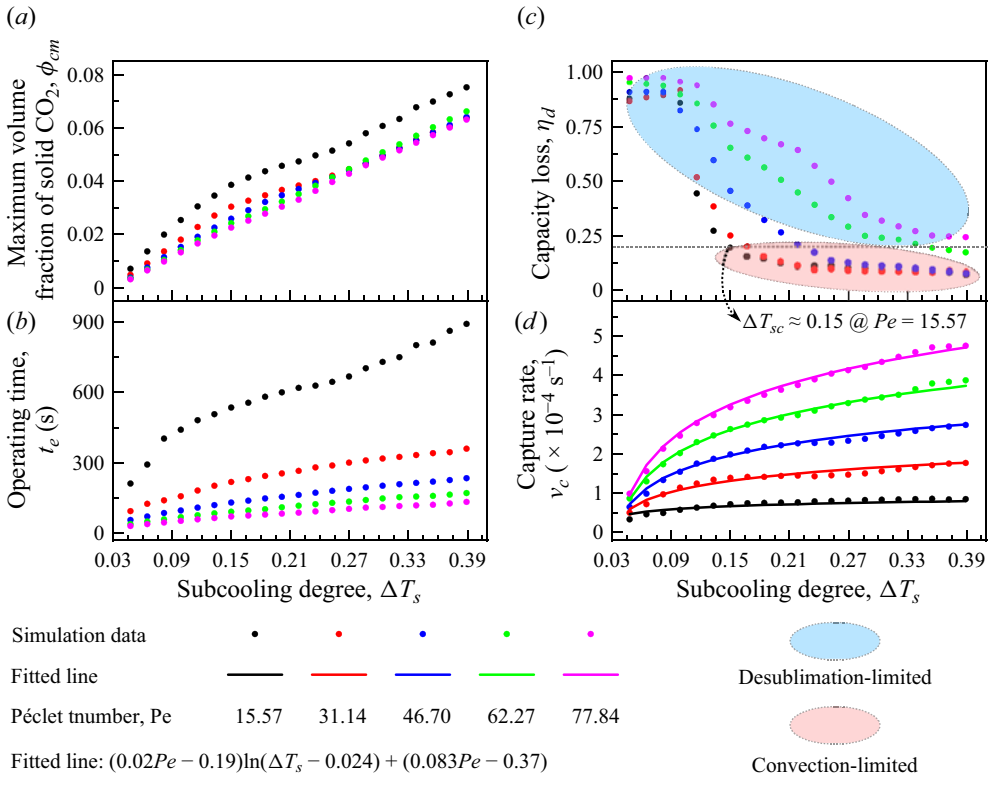

Figure 14. Analyses of CO_2 capture performance in packed-bed tests with subcooling degrees $\Delta T_s \in [0.049, 0.389]$ and Péclet numbers $Pe = 15.57, 31.14, 46.70, 62.27, 77.84$. (*a*) The maximum volume fraction of solid CO_2 (ϕ_{cm}) captured by the bed. (*b*) The operating time for CO_2 desublimation and sublimation (t_e). (*c*) The CO_2 capture capacity loss due to the time delay between the maximum and saturation points (η_d). (*d*) The CO_2 capture rate (v_c).

capacity loss). For instance, when Pe is set at 15.57, a relatively small $\Delta T_s \approx 0.09$ results in a η_d approaching 100 %, and the CCC system ceases to function. As ΔT_s grows to a significant level $\Delta T_s > 0.14$, however, a noticeable decrease in η_d to approximately 10 % becomes evident. It is because the higher ΔT_s brings about the stronger desublimation intensity and subsequently the smaller η_d. To prevent the weak desublimation and the significant η_d, ΔT_s needs to be maintained above a threshold ΔT_{sc} at a given Pe. A critical value of $\eta_{dc} = 0.2$ is set in this study to determine the value of ΔT_{sc} at each Pe (e.g. $\Delta T_{sc} \approx 0.15$ at $Pe = 15.57$). Small-ΔT_s tests (i.e. $\Delta T_s < \Delta T_{sc}$) featuring $\eta_d > 0.2$, are categorized into the desublimation-limited regime. In addition, the growing Pe amplifies the convective gas flow, yielding the severe η_d and the increased ΔT_{sc}. By combining results of v_c and η_d, both the convection-limited and desublimation-limited regimes are identified.

As mentioned above, the increasing Pe accelerates the CO_2 capture rate (v_c) but deteriorates the capture capacity (η_d). To clarify effects of Pe on the CCC system, figure 15 presents metrics (ϕ_{cm}, t_e, η_d, v_c) for tests with $\Delta T_s = 0.185$ and $Pe \in [6.23, 77.84]$. The ascending Pe (or intensified convection) results in the decreasing ϕ_{cm} and t_e (figure 15*a*,*b*). As for simulated v_c values, they fit well with the correlation obtained from figure 14(*d*), namely, $v_c = (0.02Pe - 0.19)\ln(\Delta T_s - 0.024) + (0.083Pe - 0.37)$ at $\Delta T_s = 0.185$. In contrast to the single-grain case, v_c grows continuously with Pe because the multiple

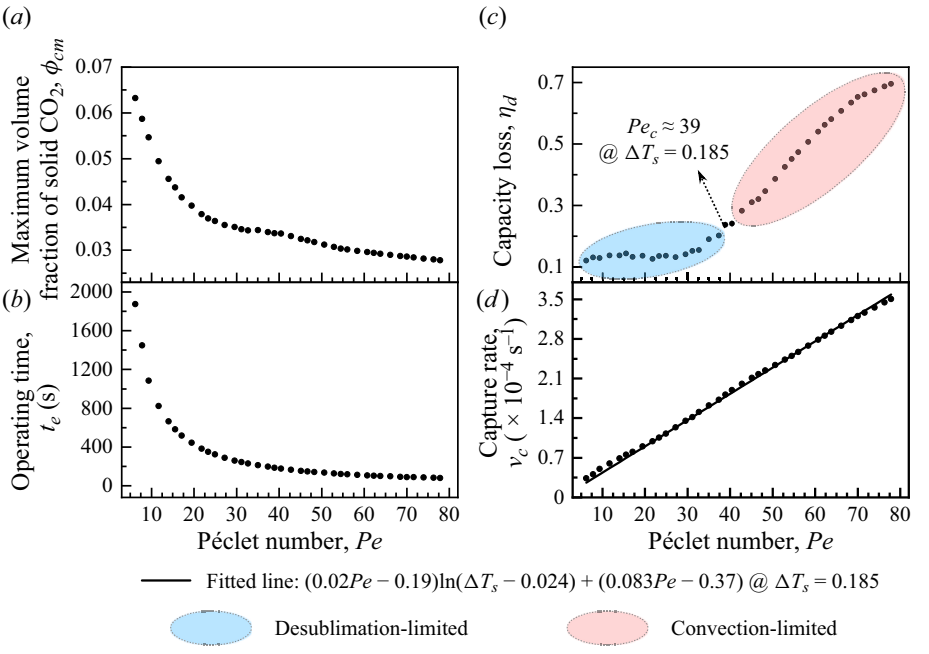

Figure 15. Analyses of CO_2 capture performance in packed-bed tests with the subcooling degree $\Delta T_s = 0.185$ and the Péclet numbers $Pe \in [6.23, 77.84]$. (*a*) The maximum volume fraction of solid CO_2 (ϕ_{cm}) captured by the bed. (*b*) The operating time for CO_2 desublimation and sublimation (t_e). (*c*) The CO_2 capacity loss due to the time delay between the maximum point and the saturation point (η_d). (*d*) The CO_2 capture rate (v_c).

cold grains are sufficient to capture CO_2. According to results of v_c, all tests are not constrained by ΔT_s and fall into the convection-limited regime. On the other side, η_d in figure 15(*c*) exhibits two distinct stages with the ascending Pe: η_d initially remains almost unchanged at around 10 % but it starts to increase sharply after a critical value of $Pe_c \approx 39$ (at $\Delta T_s = 0.185$). The intensified convection induces a shift from the convection-limited regime to the desublimation-limited one.

From results in figures 14 and 15, either a small ΔT_s or a large Pe is found to cause the desublimation-limited regime with remarkable CO_2 capture capacity loss. To show the CO_2 desublimation and sublimation properties under these two conditions, results for two tests with ($\Delta T_s = 0.006$, $Pe = 15.57$) and ($\Delta T_s = 0.185$, $Pe = 77.84$) are provided in figure 16, including distributions of solid CO_2, temperature (T), CO_2 mass fraction (Y) and their vertically averaged profiles. On the one hand, in the small-ΔT_s test ($\Delta T_s = 0.006$, $Pe = 15.57$), the desublimation rate is slow. Both the distribution of Y and the profile of $\bar{Y}_x$ support that the injected CO_2 exceeds the desublimation rate and CO_2 breaks through the bed early. On the other hand, in the large-Pe test ($\Delta T_s = 0.185$, $Pe = 77.84$), the abundant CO_2 is injected into the bed, and thus, the desublimation rate is insufficient to fully capture the injected CO_2. In these two tests, either the slow desublimation rate or the fast gas injection (or convection) make the CCC system operate in the desublimation-limited regime. Under this regime, the system reaches the saturation point too early and the cold grains are not efficiently heated up.

To comprehensively illustrate effects of ΔT_s and Pe on the CO_2 capture performance of CCC, values of η_d and v_c from simulations are plotted in the ΔT_s–Pe space (figure 17). For comparison, two grey surfaces are included for the critical value $\eta_{dc} = 0.2$ and the calculated v_{cr} from the correlation $v_c = (0.02Pe - 0.19)\ln(\Delta T_s - 0.024) + (0.083Pe -$

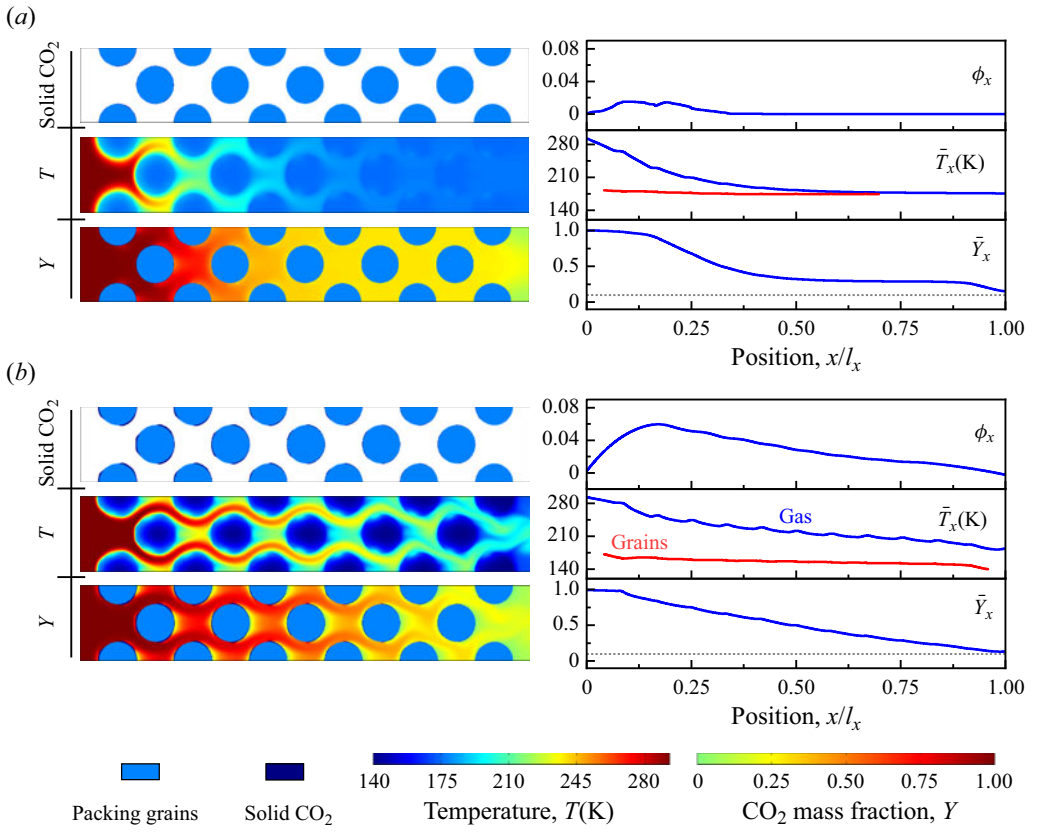

Figure 16. The CO_2 desublimation and sublimation properties in a packed bed. Contours of solid CO_2, temperature (T), CO_2 mass fraction (Y) and the corresponding vertically averaged profiles in (a) the test with the subcooling degree $\Delta T_s = 0.006$ and the Péclet number $Pe = 15.57$ at $t = 6.20$ s, and (b) the test with the subcooling degree $\Delta T_s = 0.185$ and the Péclet number $Pe = 77.84$ at $t = 8.67$ s.

0.37). The agreement between v_c and v_{cr} across all tests indicates the dominance of the convection-limited regime. Moreover, through a comparison between η_d and η_{dc}, threshold values (ΔT_{sc}, Pe_c) are obtained to delimit the domain for the desublimation-limited regime. The joint analysis of v_c and η_d produces a regime diagram in figure 18, showing distributions of the convection-limited (I) and desublimation-limited (II) regimes. The regime diagram suggests to control the gas feed rate below Pe_c and raise the subcooling degree of grains beyond ΔT_{sc}. This ensures that the CCC system operates within the convection-limited regime rather than the desublimation-limited one. Otherwise, the severe CO_2 capture capacity loss, coupled with the limited desublimation, will degrade the performance of CCC. Within the suggested parameter range, a large Pe contributes to increasing v_c while affecting η_d slightly, hence, the improved CO_2 capture performance. Besides, as ΔT_s increases, the CCC system becomes more efficient in capturing CO_2 with larger v_c and smaller η_d. However, considering the diminished improvement in the CO_2 capture performance and the escalated requirement for cooling duty, the continued rise in ΔT_s after ΔT_{sc} should be implemented with care.

The comparison between single-grain and packed-bed cases reveals their unique regime distributions and optimal operations. The desublimation-limited regime, featuring rapid CO_2 capture rate v_c, is more suited for the single-grain configuration. However, in a

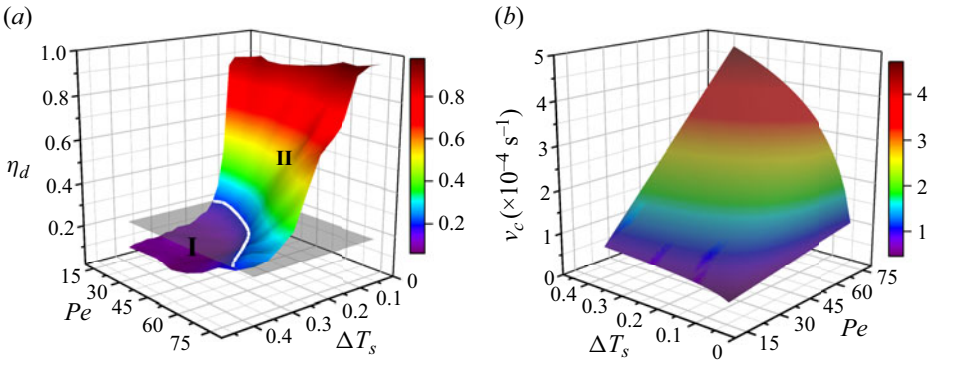

Figure 17. Analyses of (*a*) the CO_2 capacity loss (η_d) due to the time delay between the maximum point and the saturation point and (*b*) the CO_2 capture rate (v_c) in packed-bed tests with subcooling degrees $\Delta T_s \in [0.049, 0.389]$ and Péclet numbers $Pe \in [15.57, 77.84]$. Grey surfaces represent the threshold $\eta_{dc} = 0.2$ and the correlation $v_c = (0.02Pe - 0.19)\ln(\Delta T_s - 0.024) + (0.083Pe - 0.37)$. The white solid line shows the boundary between the convection-limited (I) and desublimation-limited (II) regimes.

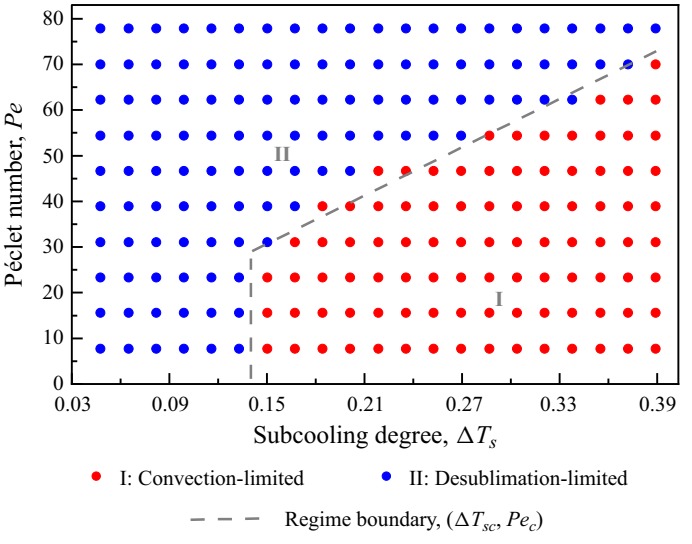

Figure 18. Analyses of CO_2 capture performance in packed-bed tests with subcooling degrees $\Delta T_s \in [0.049, 0.389]$ and Péclet numbers $Pe \in [15.57, 77.84]$. Simulation data points are plotted against ΔT_s and Pe. The grey dashed lines divide the plane into the convection-limited (I) and desublimation-limited (II) regimes.

packed bed, the CCC system operates more efficiently in the convection-limited regime, despite the high v_c in the desublimation-limited regime. This arises from the fact that the packed-bed case considers the potential loss in CO_2 capture capacity (η_d), and the limited desublimation significantly boosts η_d. On the other hand, the regime diagram for the packed-bed scenario (figure 18) illustrates an extended distribution of the convection-limited regime, when compared with the diagram for the single-grain situation (figure 10). This is attributed to the collective influence of multiple grains. These grains offer ample surface area and low temperature space, which necessitate the substantial convective CO_2 supply to sustain CO_2 desublimation. Consequently, a high Pe_c at each

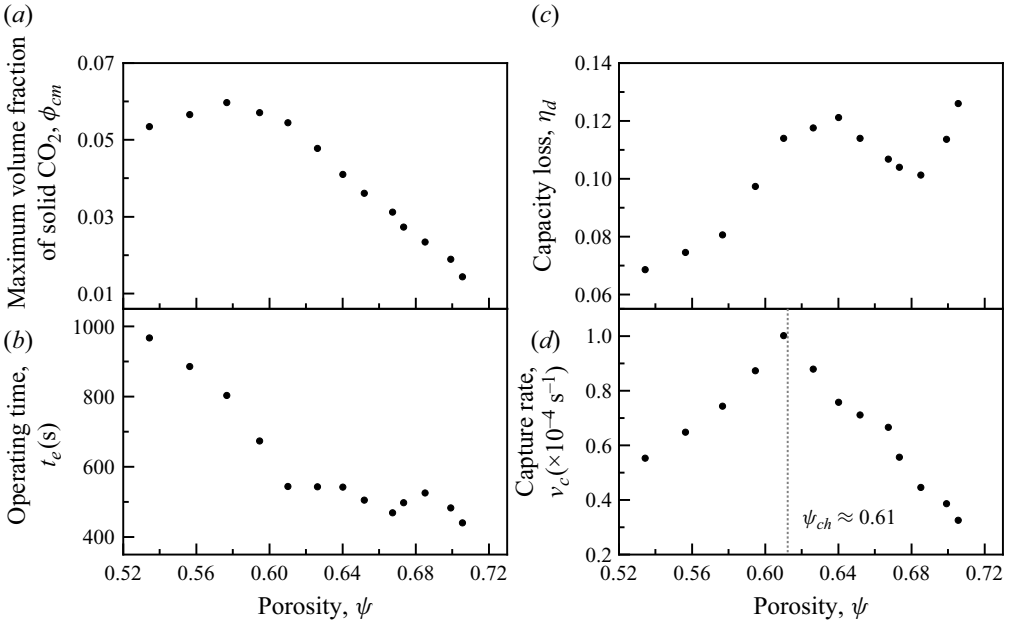

Figure 19. Analyses of CO_2 capture performance in packed-bed tests with the subcooling degree $\Delta T_s = 0.185$, Péclet number $Pe = 15.57$ and porosities $\psi \in [0.53, 0.71]$. (*a*) The maximum volume fraction of solid CO_2 (ϕ_{cm}) captured by the bed. (*b*) The operating time for CO_2 desublimation and sublimation (t_e). (*c*) The CO_2 capacity loss due to the time delay between the maximum point and the saturation point (η_d). (*d*) The CO_2 capture rate (v_c).

ΔT_s is detected in the regime diagram for the packed-bed case, forming a broad range of the convection-limited regime.

4.5. *Effects of bed structure in the packed-bed case*

In the above simulations only one porosity of the packed bed is considered as $\psi = 0.64$. In practical applications, however, ψ varies among different packed beds by adjusting the packing grain number. Attention is therefore turned to the influence of bed porosity on the CO_2 capture performance of CCC. As constructed in Appendix D, a set of bed structures with porosities $\psi \in [0.53, 0.71]$ are utilized. A test with $\Delta T_s = 0.185$ and $Pe = 15.57$ is simulated in these cryogenic beds. The obtained four metrics (ϕ_{cm}, t_e, η_d, v_c) are plotted in figure 19.

As ψ increases, there is a corresponding reduction in both the solid CO_2 captured (ϕ_{cm}) and the operating time (t_e). The primary explanation for this trend is that, in a bed with large ψ, the fluid mobility is enhanced and the gas stream is accelerated. Similar to a large-*Pe* test (figure 15), the rapid gas stream leads to the drop in both ϕ_{cm} and t_e. In the meantime, while comparing to the growing-*Pe* scenario in figure 15, two distinct findings arise from figure 19. First, with the ascending ψ, the CO_2 capture rate (v_c) increases at first but changes to decrease after a critical value $\psi_c \approx 0.61$. Different from the continuously growing v_c in figure 15(*c*), the non-monotonic variations in v_c here are driven by the two competing factors, the optimized flow channels and the diminished cold grain volume. Specifically, in the small-ψ range (i.e. $\psi < \psi_c$), the slow gas stream constrains the CO_2 capture rate v_c, and the increased ψ accelerates the flue gas flow and v_c. In the large-ψ range (i.e. $\psi > \psi_c$), however, the gas stream has been sufficiently enhanced and the limited

cold grains turn to dominate the CO_2 capture performance of CCC. The continuous rise in ψ diminishes the available cold grains for capturing CO_2 and thereby decelerates v_c. The second distinct observation from figure 15 is that the CO_2 capture capacity loss (η_d) changes non-monotonically with ψ and remains within a relatively small level as $\eta_d < 15\,\%$. This is because the injected flue gas is fixed at a given Pe and the capacity loss is limited to a certain range. These results help to draw a conclusion that a moderate bed porosity $\psi_c \approx 0.61$ is favourable for the optimal CO_2 capture performance of CCC. Compared with Pe and ΔT_s, ψ exerts marginal impacts on the CO_2 capture performance. Furthermore, effects of Pe and ΔT_s are examined at a porosity 0.64 in this study, which aligns with the recommended ϕ_c. Given these considerations, explorations into impacts of Pe and ΔT_s at other porosity values are deemed unnecessary for the scope of this study.

Overall, for a wide range of operating parameters (i.e. gas velocity, initial bed temperature and bed structures), CO_2 desublimation and sublimation during CCC have been investigated both on a single packing grain and in a packed bed. The general CO_2 desublimation and sublimation properties during the capture and recovery of CCC are successfully reproduced, which corroborate experimental observations (Tuinier *et al.* 2010; Ali *et al.* 2014). Furthermore, the quantitative analyses and parametric studies shed light on the underlying physics of CCC and also suggest optimal operating conditions.

5. Conclusions

In this work, an MRT LB model has been proposed for simulating CO_2 desublimation and sublimation during CCC at the pore scale. Compared with our previous study on CO_2 desublimation (Lei *et al.* 2023), this work newly considers CO_2 sublimation, consumption of the SCL, packed bed comprising multiple grains and non-isothermal grains over time. The performance of CCC is evaluated for different operating conditions, i.e. the initial bed temperature T_w, gas feed rate u_0 and bed structure. These conditions are characterized by dimensionless parameters such as the subcooling degree ΔT_s, Péclet number Pe and bed porosity ψ.

In the single-grain case, a test is firstly performed to reproduce CO_2 desublimation and sublimation properties. After injection, the flue gas is cooled and its component CO_2 is desublimated to generate the SCL on the grain surface. Meanwhile, the grain is heated and the SCL is sublimated for collection. A parametric study is set out to examine effects of ΔT_s and Pe. Following the rise in Pe at a constant ΔT_s, the CO_2 capture rate (v_c) increases at first but remains almost unchanged after a critical value Pe_c. These two successive stages are dominated by the weak convection and limited desublimation, respectively. Accordingly, distributions of the convection-limited (I) and desublimation-limited (II) regimes are identified in a ΔT_s–Pe space, with critical values (ΔT_{sc}, Pe_c) located on the regime boundary. In regime I ($\Delta T_s > \Delta T_{sc}$, $Pe < Pe_c$) the growing ΔT_s and Pe contribute to accelerating v_c but within a limited range. In regime II ($\Delta T_s < \Delta T_{sc}$, $Pe > Pe_c$) the optimal CO_2 capture performance (i.e. large v_c) is obtained and v_c grows monotonically with ΔT_s as $v_c = 22.56\Delta T_s - 0.76$. The non-isothermal grain yields the decreased desublimation rate over time, thereby producing different controlling regimes and CO_2 capture performance compared with our earlier study (Lei *et al.* 2023).

On the other hand, packed-bed tests are conducted for various ΔT_s, Pe and ψ, yielding CO_2 desublimation and sublimation properties, as well as the two controlling regimes (i.e. convection-limited (I) and desublimation-limited (II) regimes). A parametric study is performed to evaluate the CO_2 capture performance in terms of v_c and η_d (i.e. CO_2 capture capacity loss). The increasing ΔT_s and Pe substantially enhance v_c across

all examined packed-bed tests, following a correction $v_c = (0.02Pe - 0.19)\ln(\Delta T_s - 0.024) + (0.083Pe - 0.37)$. This is driven by the existence of multiple grains that offer a substantial cold surface for capturing CO_2. Subsequently, the convective CO_2 supply is insufficient and CCC operates in regime I. In addition, either a diminished ΔT_s or an elevated Pe is found to result in the decreased desublimation rate relative to the convective CO_2 supply, thus exacerbating η_d and bringing about regime II. By analysing v_c and η_d, a regime diagram is constructed to delineate distributions of regimes I and II in a ΔT_s–Pe space, together with the regime boundary and threshold values (ΔT_{sc}, Pe_c). In contrast to the single-grain scenario, regime I is broadened because the multiple cold grains require amplified convection, and regime I is more advantageous due to the diminished η_d. Finally, following the growing ψ, η_d changes slightly and v_c varies non-monotonically with a peak value at $\psi_c \approx 0.61$. This is attributed to the two competing mechanisms introduced by the ascending ψ: improved fluid mobility and decreased cold grain areas. To optimize the performance of CCC (i.e. large v_c and small η_d) within regime I, it is recommended to pursue the high Pe, large ΔT_s and moderate ψ_c. In both the single-grain and packed cases, a high ΔT_s should be exercised with caution since it boosts the cooling duty significantly.

To conclude, the proposed LB model is successful in reproducing CO_2 desublimation and sublimation properties during CCC, over extensive operating conditions. For the operation of CCC, the present findings advance the knowledge base and offer valuable insights into the underlying physics. This study thus illustrates the LB modelling capability to facilitate the optimization and commercial development of CCC, which is a promising technology for combating climate change. For a thorough evaluation of CCC performance, future research should incorporate an in-depth analysis of the cooling step. This would entail a detailed assessment of the cryogenic temperature by taking into account the cooling duty. Furthermore, given the multicomponent nature of flue gas emitted from industrial processes, it is imperative to investigate the transport of multiple gaseous components, e.g. CO_2, N_2, H_2O, CH_4. The interplay between these components, coupled with their distinct freezing points, may affect the optimal operational conditions. Additionally, due to the presence of H_2O, the incorporation of a dehydration unit prior to CO_2 purification is necessary, and an evaluation of its impact on CCC performance is essential.

Supplementary material. Supplementary material is available at https://doi.org/10.1017/jfm.2024.351.

Funding. This work was supported by the UK Engineering and Physical Sciences Research Council (EPSRC) under the grant no. EP/W026260/1, as well as by King Abdullah University of Science and Technology (KAUST). ARCHER2 supercomputing resources provided by EPSRC under the project 'UK Consortium on Mesoscale Engineering Sciences (UKCOMES)' (grant no. EP/X035875/1) are gratefully acknowledged. This work made use of computational support by CoSeC, the Computational Science Centre for Research Communities, through UKCOMES.

Declaration of interests. The authors report no conflict of interest.

Author ORCIDs.
Timan Lei https://orcid.org/0000-0002-8031-6632;
Kai H. Luo https://orcid.org/0000-0003-4023-7259;
Francisco E. Hernández Pérez https://orcid.org/0000-0001-7906-8646;
Junyu Yang https://orcid.org/0000-0002-7771-1308;
Juan Restrepo Cano https://orcid.org/0000-0001-8831-2735;
Hong G. Im https://orcid.org/0000-0001-7080-1266.

Appendix A. Transformation details in the MRT model

Our earlier research suggested that 2-D simulations are adequate for examining CO_2 desublimation regimes (Lei *et al.* 2023). Building upon this premise, this study is dedicated to modelling CO_2 desublimation and sublimation during CCC in two dimensions. Accordingly, the 2-D nine-velocity scheme of the proposed MRT LB model is employed for simulations. The discrete velocities $\boldsymbol{e}_i$ and weight coefficients w_i are (Guo & Shu 2013)

$$\left.\begin{aligned} \boldsymbol{e}_i &= e\,(0,\ 0)\,, && w_i = 4/9,\ i = 0, \\ \boldsymbol{e}_i &= e\left(\cos\frac{(i-1)\pi}{2}, \sin\frac{(i-1)\pi}{2}\right), && w_i = 1/9,\ i = 1-4, \\ \boldsymbol{e}_i &= \sqrt{2}e\left(\cos\frac{(2i-1)\pi}{4}, \sin\frac{(2i-1)\pi}{4}\right), && w_i = 1/36,\ i = 5-8, \end{aligned}\right\} \tag{A1}$$

with $e = 1$ in this study. To reduce compressibility errors, the equilibrium distribution functions are given as (Lei *et al.* 2023)

$$f_i^{eq} = w_i\left[\rho_g + \rho_p\left(\frac{\boldsymbol{e}_i\cdot\boldsymbol{u}}{c_s^2} + \frac{(\boldsymbol{e}_i\cdot\boldsymbol{u})^2}{2c_s^4} - \frac{\boldsymbol{u}^2}{2c_s^2}\right)\right], \tag{A2}$$

$$g_i^{eq} = w_i Y\left[1 + \frac{\boldsymbol{e}_i\cdot\boldsymbol{u}}{c_s^2} + \frac{(\boldsymbol{e}_i\cdot\boldsymbol{u})^2}{2c_s^4} - \frac{\boldsymbol{u}^2}{2c_s^2}\right], \tag{A3}$$

$$h_i^{eq} = w_i T\left[1 + \frac{\boldsymbol{e}_i\cdot\boldsymbol{u}}{c_s^2} + \frac{(\boldsymbol{e}_i\cdot\boldsymbol{u})^2}{2c_s^4} - \frac{\boldsymbol{u}^2}{2c_s^2}\right]. \tag{A4}$$

To avoid discrete lattice effects, the distribution function $\bar{F}_{T,i}$ is (Guo & Zhao 2002; Shi & Guo 2009)

$$\bar{F}_{T,i} = w_i F_T\left(1 + \frac{\boldsymbol{e}_i\cdot\boldsymbol{u}}{c_s^2}\frac{\tau_t - 0.5}{\tau_t}\right), \tag{A5}$$

with τ_t being the relaxation time.

The transformation matrix $\boldsymbol{M}$ is

$$\boldsymbol{M} = \begin{bmatrix} 1 & 1 & 1 & 1 & 1 & 1 & 1 & 1 & 1 \\ -4 & -1 & -1 & -1 & -1 & 2 & 2 & 2 & 2 \\ 4 & -2 & -2 & -2 & -2 & 1 & 1 & 1 & 1 \\ 0 & 1 & 0 & -1 & 0 & 1 & -1 & -1 & 1 \\ 0 & -2 & 0 & 2 & 0 & 1 & -1 & -1 & 1 \\ 0 & 0 & 1 & 0 & -1 & 1 & 1 & -1 & -1 \\ 0 & 0 & -2 & 0 & 2 & 1 & 1 & -1 & -1 \\ 0 & 1 & -1 & 1 & -1 & 0 & 0 & 0 & 0 \\ 0 & 0 & 0 & 0 & 0 & 1 & -1 & 1 & -1 \end{bmatrix}, \tag{A6}$$

$\boldsymbol{M}$ maps distribution functions from the physical space $\boldsymbol{\psi}$ to the moment space as $\hat{\boldsymbol{\psi}} = \boldsymbol{M}\cdot\boldsymbol{\psi}$. With this transformation, evolution equations (3.3)–(3.5) are performed in the moment

space as

$$\hat{\boldsymbol{f}}\left(\boldsymbol{x}+\boldsymbol{e}_i\delta_t, t+\delta_t\right)=\hat{\boldsymbol{f}}\left(\boldsymbol{x}, t\right)-\boldsymbol{S}\left[\hat{\boldsymbol{f}}\left(\boldsymbol{x}, t\right)-\hat{\boldsymbol{f}}^{eq}\left(\boldsymbol{x}, t\right)\right], \tag{A7}$$

$$\hat{\boldsymbol{g}}\left(\boldsymbol{x}+\boldsymbol{e}_i\delta_t, t+\delta_t\right)=\hat{\boldsymbol{g}}\left(\boldsymbol{x}, t\right)-\boldsymbol{S}_y\left[\hat{\boldsymbol{g}}\left(\boldsymbol{x}, t\right)-\hat{\boldsymbol{g}}^{eq}\left(\boldsymbol{x}, t\right)\right], \tag{A8}$$

$$\hat{\boldsymbol{h}}\left(\boldsymbol{x}+\boldsymbol{e}_i\delta_t, t+\delta_t\right)=\hat{\boldsymbol{h}}\left(\boldsymbol{x}, t\right)-\boldsymbol{S}_t\left[\hat{\boldsymbol{h}}\left(\boldsymbol{x}, t\right)-\hat{\boldsymbol{h}}^{eq}\left(\boldsymbol{x}, t\right)\right]+\delta_t\hat{\boldsymbol{F}}_T+0.5\delta_t^2\partial_t\hat{\boldsymbol{F}}_T. \tag{A9}$$

Through the Chapman–Enskog analysis on the proposed LB equations, the governing equations can be recovered with the relaxation times τ, τ_y and τ_t being

$$\nu=c_s^2\left(\tau-0.5\right)\delta_t, \quad D=c_s^2\left(\tau_y-0.5\right)\delta_t, \quad \alpha=c_s^2\left(\tau_t-0.5\right)\delta_t, \tag{A10a–c}$$

as well as the gradient terms of temperature (∇T) being (Lei, Meng & Guo 2017; Lei *et al.* 2021)

$$\nabla_x T=-\frac{\hat{h}_3-Tu+0.5\delta_t F_T u}{c_s^2\tau_t\delta_t}, \quad \nabla_y T=-\frac{\hat{h}_5-Tv+0.5\delta_t F_T v}{c_s^2\tau_t\delta_t}. \tag{A11a,b}$$

Except for these calculations, the gradient term in (3.2*a–c*) is determined by using the isotropic central scheme as (Guo, Zheng & Shi 2011)

$$\nabla\left(\rho c_p\right)=\sum_i\frac{w_i\boldsymbol{e}_i\rho c_p\left(\boldsymbol{x}+\boldsymbol{e}_i\delta_t\right)}{c_s^2\delta_t}. \tag{A12}$$

It is emphasized that the proposed MRT LB model can be easily extended to three dimensions through the modification of discrete velocities $\boldsymbol{e}_i$, weight coefficients w_i and the transformation matrix $\boldsymbol{M}$ into their three-dimensional (3-D) counterparts. More details of 3-D models and simulation results can be found in Appendix E, which demonstrated that the CO_2 desublimation and sublimation properties are comparable in both 2-D and 3-D simulations.

Appendix B. Boundary treatment

Boundary conditions at the four external boundaries of the computational domain in figure 2 are set as follows. First, from the inlet ($x=0$), the flue gas is fed into the domain at a given operating condition. The gas compositions, temperature, pressure and velocity are accordingly set as specified values. Then, at the outlet ($x=l_x$), a fully developed flow is considered so that the flue gas flows out freely. The zero-gradient velocity and the no-flux temperature and mass fractions are applied there. Finally, at the bottom ($y=0$) and top ($y=l_y$), the periodic conditions are imposed. These boundaries are mathematically described by

$$x=0: \quad u=u_0, v=0, Y=Y_0, T=T_0, \tag{B1}$$

$$x=l_x: \quad \nabla u=\nabla v=\boldsymbol{0}, \nabla Y=\boldsymbol{0}, \nabla T=\boldsymbol{0}, \tag{B2}$$

$$y=0, l_y: \quad \boldsymbol{u}_{y=0}=\boldsymbol{u}_{y=l_y}, Y_{y=0}=Y_{y=l_y}, T_{y=0}=T_{y=l_y}. \tag{B3}$$

To obtain enclosing solutions of (2.8)–(2.10) and (3.1), these external boundaries should be implemented by applying LB boundary schemes. At the inlet (B1) and the outlet (B2), the non-equilibrium extrapolation boundary scheme is utilized to reconstruct the unknown distribution functions (Guo & Shu 2013). At the periodic top and bottom boundaries (B3),

the outgoing distribution functions from the top re-enter the domain from the bottom, and *vice versa* (Guo & Shu 2013).

On the other hand, at the internal inactive gas–solid interface I_n without CO_2 desublimation and sublimation, the no-flux condition is applied for mass conservation. Thus, the boundary conditions are

$$\boldsymbol{u}^{I_n} = (0, 0)\,, \tag{B4}$$

$$\nabla Y^{I_n} = 0, \tag{B5}$$

$$\left.\begin{aligned} T^{I_n,+} &= T^{I_n,-}, \\ \boldsymbol{n}\cdot\left(k\nabla T + \rho c_p \boldsymbol{u} T\right)^{I_n,+} &= \boldsymbol{n}\cdot\left(k\nabla T + \rho c_p \boldsymbol{u} T\right)^{I_n,-}. \end{aligned}\right\} \tag{B6}$$

The LB boundary schemes are built to enforce the internal interface I_n without CO_2 desublimation and sublimation (i.e. (B4)–(B6)). The no-slip velocity in (B4) and the conjugate heat transfer in (B6) are achieved as conducted at active interface $I_{d,s}$ in § 3.2. Differently, the no-flux mass fraction in (B5) is enforced by the halfway bounce-back scheme. For addressing the no-slip velocity and no-flux mass fraction conditions, the unknown distribution functions are calculated as (Zhang *et al.* 2012)

$$f_{\bar{i}}\left(\boldsymbol{x}_g, t+\delta_t\right) = f_i'\left(\boldsymbol{x}_g, t\right), \tag{B7}$$

$$g_{\bar{i}}\left(\boldsymbol{x}_g, t+\delta_t\right) = g_i'\left(\boldsymbol{x}_g, t\right). \tag{B8}$$

Appendix C. Model validation

For simulating CO_2 desublimation during CCC, we have recently developed an LB model (Lei *et al.* 2023). As an extension, the present LB model newly introduces the sublimation of solid CO_2 and the variation of packing grains' temperature. In our recent work, benchmark problems with widely accepted or analytical solutions have been simulated to test key sub-models of the proposed LB model, including the boundary scheme for mass conservation at the active fluid–solid interface, the source term for conjugate heat transfer and the VOP scheme for updating solid CO_2 (Lei *et al.* 2023). For brevity, these validation details are not repeatedly introduced here. Therefore, we focus on testing the newly introduced CO_2 sublimation and temperature variations of packing grains in this section. The CO_2 desublimation and sublimation in a packed bed fed with flue gas is considered. A cryogenic bed is introduced as shown in figure 20(*a*). The computational domain is $0 \le x \le l_x$ and $0 \le y \le l_y$, which is packed with multiple grains. From the left inlet, the flue gas is injected into the bed at the initial condition (T_0, Y_0, u_0, p_0). The injected CO_2 deposits on the surface of packing grains and the bed gradually becomes heated by the injected flue gas. Once the bed reaches saturation, the injected CO_2 leaves the domain from the right outlet without phase change.

Based on such a system, we simulate the CO_2 desublimation and sublimation processes. Our simulations consider both the counter-current and co-current flow configurations in § 3.1 of Ali *et al.* (2014), with which the same desublimation and sublimation conditions are selected. Specifically, the bed size $l_x \times l_y = 0.46\,\mathrm{m} \times 0.0418\,\mathrm{m}$, the porosity $\psi = 0.637$, the inlet flue gas temperature $T_0 = 293\,\mathrm{K}$, the inlet CO_2 mass fraction $Y_0 = 1$ and the gas pressure $p_0 = 1\,\mathrm{atm}$. From the inlet to the outlet, the initial bed temperature T_w decreases for the counter-current flow configuration and increases for the co-current flow configuration. The thermophysical properties of the gas and the solid phases are set as in our simulations in § 4. A mesh of size 500×5500 is applied. The

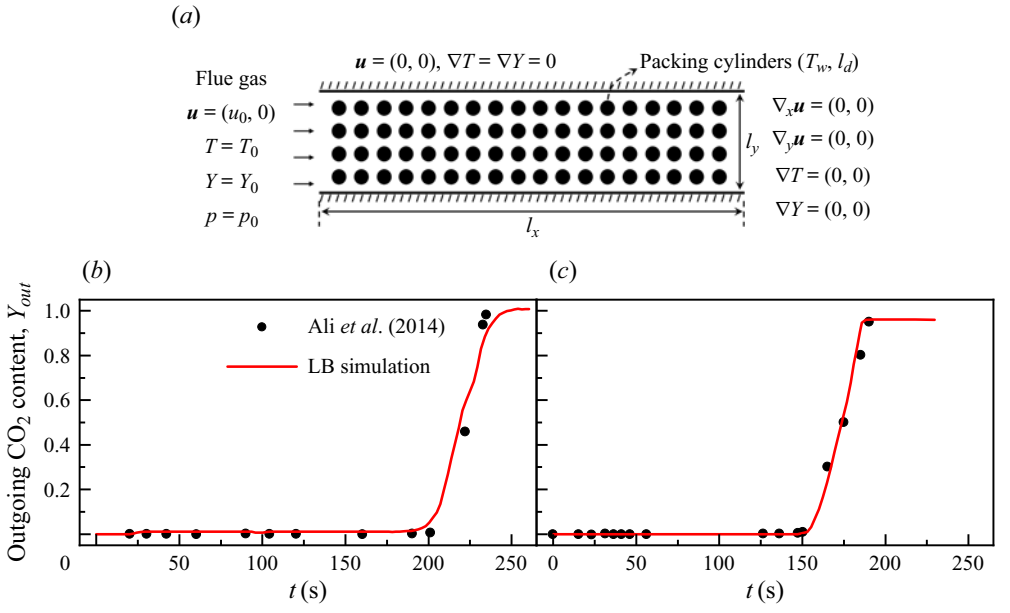

Figure 20. Model validation of CO_2 desublimation and sublimation in a cryogenic packed bed with the flue gas feed flow. (*a*) Computational domain and boundary conditions. Comparison of the outgoing CO_2 content between the present numerical results and the experimental measurements in Ali *et al.* (2014) for (*a*) counter-current flow configuration and (*b*) co-current flow configuration.

outgoing CO_2 at the outlet is recorded and compared with experimental data in Ali *et al.* (2014) to examine the reliability of the present LB model. The calculated outgoing CO_2 are plotted against time in figure 20(*b*,*c*). As can be seen, the present LB model can reproduce the same CO_2 capture performance as the experiments for different flow configurations. Therefore, it demonstrates that the present LB model is accurate for simulating the CO_2 desublimation and sublimation in a packed bed.

Appendix D. Simulation parameters

For simulations of CO_2 desublimation and sublimation in this study, the range of initial bed temperature $T_w \in [80\,\mathrm{K}, 180\,\mathrm{K}]$ and the range of gas injection velocity $u_0 \in [1.22 \times 10^{-3}\,\mathrm{m\,s^{-1}}, 6.10 \times 10^{-2}\,\mathrm{m\,s^{-1}}]$ are covered. The corresponding subcooling degree of the packing grain $\Delta T_s = (T_f - T_w)/T_0$ and Péclet number $Pe = (l_y u_0)/D$ are listed in table 2.

In order to explore effects of the packed bed porosity (ψ) on the performance of CCC, a series of packed bed structures are considered. As shown in figure 21, different 2-D structures are constructed to represent cross-sections of 3-D packed beds along the gas flow direction. Based on these artificially produced profiles, effects of packed bed structure are explored. All bed cross-sections consist of regularly distributed packing grains and share the same domain size and grain diameter, namely, length $l_x = 124.8\,\mathrm{mm}$, width $l_y = 20.8\,\mathrm{mm}$ and grain diameter $l_d = 10.0\,\mathrm{mm}$; however, they vary in grain distributions (r_x, r_y) to generate different porosities ψ. Key parameters are provided in table 2. Note that, in accordance with the previous experimental set-up (Ali *et al.* 2014), all cryogenic beds considered in this study are filled with glass packing materials. Other packing materials characterized by the higher $\rho c_{p,c}$ and smaller α_c are expected to improve the CO_2 capture performance of CCC.

https://doi.org/10.1017/jfm.2024.351 Published online by Cambridge University Press

T_w	80	85	90	95	100	105	110	115	120	125	130	135	140	145
ΔT_s	0.389	0.372	0.355	0.338	0.321	0.304	0.287	0.270	0.253	0.236	0.219	0.202	0.185	0.168
	150	155	160	165	170	175	180	—	—	—	—	—	—	—
	0.151	0.134	0.117	0.100	0.083	0.066	0.049	—	—	—	—	—	—	—
u_0	0.122	0.305	0.488	0.610	0.732	0.915	1.098	1.220	1.342	1.525	1.708	1.830	1.952	2.135
Pe	1.55	3.89	6.23	7.78	9.34	11.68	14.01	15.57	17.12	19.46	21.80	23.35	24.91	27.24
	2.318	2.440	2.562	2.745	2.928	3.050	3.172	3.355	3.538	3.660	3.782	3.965	4.148	4.270
	29.58	31.14	32.69	35.03	37.36	38.92	40.48	42.81	45.15	46.70	48.26	50.60	52.93	54.49
	4.392	4.575	4.758	4.880	5.002	5.185	5.368	5.490	5.612	5.795	5.978	6.100	—	—
	56.05	58.38	60.72	62.27	63.82	66.16	68.50	70.06	71.61	73.95	76.28	77.84	—	—
r_x	15.9	16.7	17.6	18.4	19.2	20.0	20.8	21.6	22.4	23.2	24.1	24.9	25.7	—
ψ	0.53	0.56	0.58	0.60	0.61	0.63	0.64	0.65	0.67	0.67	0.69	0.70	0.71	—

Table 2. Values of the initial bed temperature T_w (K), gas feed rate $u_0 (\times 10^{-2}\ \mathrm{m\,s^{-1}})$ and grain position r_x (m) (with $r_y = l_y$), as well as the corresponding subcooling degree ΔT_s, Péclet number Pe and bed porosity ψ.

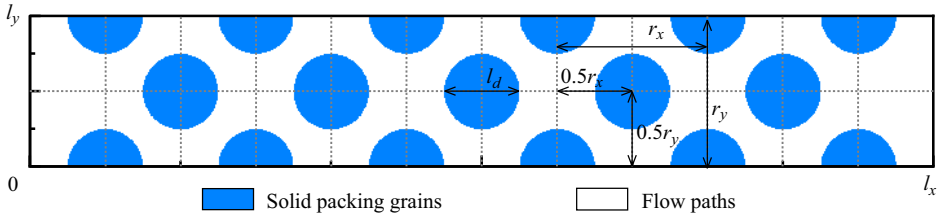

Figure 21. The schematic diagrams of the cryogenic packed bed.

Appendix E. Comparison between 2-D and 3-D simulations

This research focuses on simulating the desublimation and sublimation of CO_2 during CCC in two dimensions. To validate that the current 2-D results are applicable to 3-D implementations of CCC, this section extends the proposed LB model to simulate 3-D processes of CO_2 desublimation and sublimation. Accordingly, the discrete velocities e_i, weight coefficients w_i and the transformation matrix $\boldsymbol{M}$ are set as their 3-D counterparts (Lei *et al.* 2023).

$$\boldsymbol{e}_i = e\begin{bmatrix} 0 & 1 & -1 & 0 & 0 & 0 & 0 & 1 & -1 & 1 & -1 & 1 & -1 & -1 & 1 \\ 0 & 0 & 0 & 1 & -1 & 0 & 0 & 1 & -1 & 1 & -1 & -1 & 1 & 1 & -1 \\ 0 & 0 & 0 & 0 & 0 & 1 & -1 & 1 & -1 & -1 & 1 & 1 & -1 & 1 & -1 \end{bmatrix}, \tag{E1}$$

$$w_i = \begin{cases} 2/9, & i = 0, \\ 1/9, & i = 1\text{–}6, \\ 1/72, & i = 7\text{–}14, \end{cases} \tag{E2}$$

$$\boldsymbol{M} = \begin{bmatrix} 1 & 1 & 1 & 1 & 1 & 1 & 1 & 1 & 1 & 1 & 1 & 1 & 1 & 1 & 1 \\ -2 & -1 & -1 & -1 & -1 & -1 & -1 & 1 & 1 & 1 & 1 & 1 & 1 & 1 & 1 \\ 16 & -4 & -4 & -4 & -4 & -4 & -4 & 1 & 1 & 1 & 1 & 1 & 1 & 1 & 1 \\ 0 & 1 & -1 & 0 & 0 & 0 & 0 & 1 & -1 & 1 & -1 & 1 & -1 & 1 & -1 \\ 0 & -4 & 4 & 0 & 0 & 0 & 0 & 1 & -1 & 1 & -1 & 1 & -1 & 1 & -1 \\ 0 & 0 & 0 & 1 & -1 & 0 & 0 & 1 & 1 & -1 & -1 & 1 & 1 & -1 & -1 \\ 0 & 0 & 0 & -4 & 4 & 0 & 0 & 1 & 1 & -1 & -1 & 1 & 1 & -1 & -1 \\ 0 & 0 & 0 & 0 & 0 & 1 & -1 & 1 & 1 & 1 & 1 & -1 & -1 & -1 & -1 \\ 0 & 0 & 0 & 0 & 0 & -4 & 4 & 1 & 1 & 1 & 1 & -1 & -1 & -1 & -1 \\ 0 & 2 & 2 & -1 & -1 & -1 & -1 & 0 & 0 & 0 & 0 & 0 & 0 & 0 & 0 \\ 0 & 0 & 0 & 1 & 1 & -1 & -1 & 0 & 0 & 0 & 0 & 0 & 0 & 0 & 0 \\ 0 & 0 & 0 & 0 & 0 & 0 & 0 & 1 & -1 & -1 & 1 & 1 & -1 & -1 & 1 \\ 0 & 0 & 0 & 0 & 0 & 0 & 0 & 1 & 1 & -1 & -1 & -1 & -1 & 1 & 1 \\ 0 & 0 & 0 & 0 & 0 & 0 & 0 & 1 & -1 & 1 & -1 & -1 & 1 & -1 & 1 \\ 0 & 0 & 0 & 0 & 0 & 0 & 0 & 1 & -1 & -1 & 1 & -1 & 1 & 1 & -1 \end{bmatrix}. \tag{E3}$$

Using this 3-D 15-velocity LB model, the single-grain test in § 4.1 is re-simulated within a computational domain of $l_{sx} \times l_{sy} \times l_{sz} = 14.7\,\text{mm} \times 14.7\,\text{mm} \times 0.7\,\text{mm}$ (i.e. $640 \times 640 \times 30$). The boundary and operating conditions are set as described in § 4.1, incorporating periodic conditions along the z axis. The CO_2 desublimation and sublimation properties are provided in figure 22, which details both the volume fraction of the captured solid CO_2 (ϕ_c) and the contours of solid CO_2.

The simulation results show that the CO_2 desublimation and sublimation characteristics observed in 2-D simulations align with those from 3-D simulations. Both 2-D and 3-D

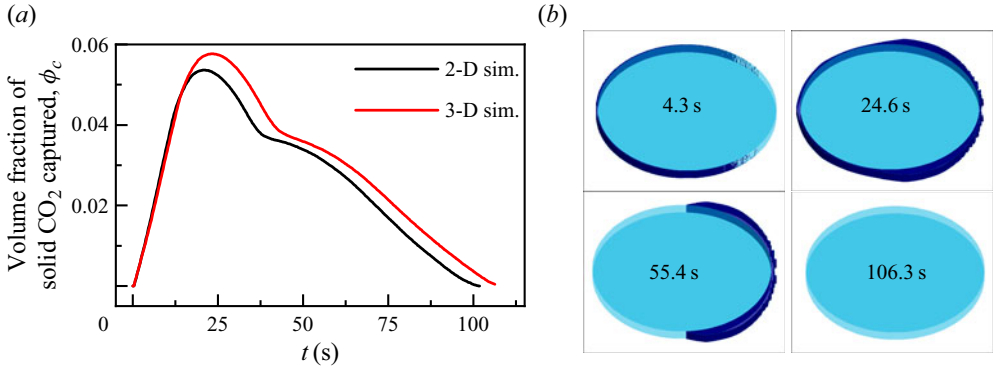

Figure 22. Comparison between 2-D and 3-D simulations. Temporal evolutions of (*a*) volume fraction of the captured solid CO_2 (ϕ_c) and (*b*) contours of solid CO_2.

simulations capture the generation and consumption of solid CO_2, successfully identify the peak value of solid CO_2 and reproduce the CO_2 capture and recovery steps of CCC. Besides these shared characteristics, minor variances are also noted between the 2-D and 3-D outcomes. As explained in Lei *et al.* (2023), the extra reaction surface and growth direction introduced by the 3-D structure are responsible for these discrepancies. However, the 2-D simulation effectively replicates the CO_2 capture and recovery phases of CCC, thus confirming the credibility of the current study.

References

BIN AB HALIM, M.A.R. 2013 Multiple cryogenic packed bed dehydration and separation of CO_2 and hydrocarbons from natural gas. Bachelor's thesis, Universiti Teknologi PETRONAS.

ALI, A., MAQSOOD, K., REDZA, A., HII, K., SHARIFF, A.B.M. & GANGULY, S. 2016 Performance enhancement using multiple cryogenic desublimation based pipeline network during dehydration and carbon capture from natural gas. *Chem. Engng Res. Des.* **109**, 519–531.

ALI, A., MAQSOOD, K., SYAHERA, N., SHARIFF, A.B.M. & GANGULY, S. 2014 Energy minimization in cryogenic packed beds during purification of natural gas with high CO_2 content. *Chem. Engng Technol.* **37** (10), 1675–1685.

BABAR, M., BUSTAM, M.A., ALI, A. & MAULUD, A.S. 2018 Identification and quantification of CO_2 solidification in cryogenic CO_2 capture from natural gas. *Intl J. Autom. Mech. Engng* **15** (2), 5367.

BABAR, M., MUKHTAR, A., MUBASHIR, M., SAQIB, S., ULLAH, S., QUDDUSI, A.H.A., BUSTAM, M.A. & SHOW, P.L. 2021 Development of a novel switched packed bed process for cryogenic CO_2 capture from natural gas. *Process Saf. Environ. Prot.* **147**, 878–887.

CANN, D. & FONT-PALMA, C. 2023 Evaluation of mathematical models for CO_2 frost formation in a cryogenic moving bed. *Energies* **16** (5), 2314.

CANN, D., FONT-PALMA, C. & WILLSON, P. 2021*a* Experimental analysis of CO_2 frost front behaviour in moving packed beds for cryogenic CO_2 capture. *Intl J. Greenh. Gas Control* **107**, 103291.

CANN, D., FONT-PALMA, C. & WILLSON, P. 2021*b* Moving packed beds for cryogenic CO_2 capture: analysis of packing material and bed precooling. *Carbon Capture Sci. Technol.* **1**, 100017.

CHEN, L., HE, A., ZHAO, J.L., KANG, Q.J., LI, Z.Y., CARMELIET, J., SHIKAZONO, N. & TAO, W.Q. 2022 Pore-scale modeling of complex transport phenomena in porous media. *Prog. Energy Combust. Sci.* **88**, 100968.

CHEN, L., KANG, Q.J., CAREY, B. & TAO, W.Q. 2014 Pore-scale study of diffusion-reaction processes involving dissolution and precipitation using the lattice Boltzmann method. *Intl J. Heat Mass Transfer* **75**, 483–496.

CHEN, L., ZHANG, R.Y., KANG, Q.J. & TAO, W.Q. 2020 Pore-scale study of pore-ionomer interfacial reactive transport processes in proton exchange membrane fuel cell catalyst layer. *Chem. Engng J.* **391**, 123590.

DEBNATH, B., MUKHERJEE, A., MULLICK, A., GHOSHDASTIDAR, S., GANGULY, S. & KARGUPTA, K. 2019 Desublimation based separation of CO_2 inside a cryogenic packed bed: performance mapping with the spatiotemporal evolution of CO_2 frost. *Chem. Engng Res. Des.* **146**, 166–181.

FONT-PALMA, C. 2021 Is carbon capture a viable solution to decarbonise the shipping industry? In *The 11th International Trondheim Conference on* CO_2 *Capture, Transport and Storage* (ed. N.A. Røkke (SINTEF) and Hanna K. Knuutila (NTNU)). SINTEF Academic Press.

FONT-PALMA, C., CANN, D. & UDEMU, C. 2021 Review of cryogenic carbon capture innovations and their potential applications. *J. Carbon Res.* **7** (3), 58.

GALLUCCI, F. & VAN SINT ANNALAND, M. 2015 *Process Intensification for Sustainable Energy Conversion*. John Wiley & Sons.

GUO, Z.L. & SHU, C. 2013 *Lattice Boltzmann Method and its Applications in Engineering*. World Scientific Publisher.

GUO, Z.L. & ZHAO, T.S. 2002 Lattice Boltzmann model for incompressible flows through porous media. *Phys. Rev.* E **66** (3), 036304.

GUO, Z.L., ZHENG, C.G. & SHI, B.C. 2011 Force imbalance in lattice Boltzmann equation for two-phase flows. *Phys. Rev.* E **83** (3), 036707.

HE, Y.L., LIU, Q., LI, Q. & TAO, W.Q. 2019 Lattice Boltzmann methods for single-phase and solid-liquid phase-change heat transfer in porous media: a review. *Intl J. Heat Mass Transfer* **129**, 160–197.

HU, C.L., XU, K. & YANG, Y.T. 2023 Effects of the geothermal gradient on the convective dissolution in CO_2 sequestration. *J. Fluid Mech.* **963**, A23.

KANG, Q.J., CHEN, L., VALOCCHI, A.J. & VISWANATHAN, H.S. 2014 Pore-scale study of dissolution-induced changes in permeability and porosity of porous media. *J. Hydrol.* **517**, 1049–1055.

KANG, Q.J., LICHTNER, P.C. & ZHANG, D.X. 2006 Lattice Boltzmann pore-scale model for multicomponent reactive transport in porous media. *J. Geophys. Res.: Solid Earth* **111** (B5), B05203.

KARANI, H. & HUBER, C. 2015 Lattice Boltzmann formulation for conjugate heat transfer in heterogeneous media. *Phys. Rev.* E **91** (2), 023304.

LEI, T. & LUO, K.H. 2019 Pore-scale study of dissolution-driven density instability with reaction $A + B \rightarrow C$ in porous media. *Phys. Rev. Fluids* **4** (6), 063907.

LEI, T. & LUO, K.H. 2021 Pore-scale simulation of miscible viscous fingering with dissolution reaction in porous media. *Phys. Fluids* **33** (3), 034134.

LEI, T., LUO, K.H., HERNÁNDEZ PÉREZ, F.E., WANG, G., WANG, Z., RESTREPO CANO, J. & IM, H.G. 2023 Study of CO_2 desublimation during cryogenic carbon capture using the lattice Boltzmann method. *J. Fluid Mech.* **964**, A1.

LEI, T., LUO, K.H. & WU, D. 2019 Generalized lattice Boltzmann model for frosting. *Phys. Rev.* E **99** (5), 053301.

LEI, T., MENG, X.H. & GUO, Z.L. 2017 Pore-scale study on reactive mixing of miscible solutions with viscous fingering in porous media. *Comput. Fluids* **155**, 146–160.

LEI, T., WANG, Z. & LUO, K.H. 2021 Study of pore-scale coke combustion in porous media using lattice Boltzmann method. *Combust. Flame* **225**, 104–119.

LETELIER, J.A., ULLOA, H.N., LEYRER, J. & ORTEGA, J.H. 2023 Scaling CO_2-brine mixing in permeable media via analogue models. *J. Fluid Mech.* **962**, A8.

LI, Q., LUO, K.H., KANG, Q.J., HE, Y.L., CHEN, Q. & LIU, Q. 2016 Lattice Boltzmann methods for multiphase flow and phase-change heat transfer. *Prog. Energy Combust. Sci.* **52**, 62–105.

LI, Z.X. & SHAN, X.W. 2023 Body-force modelling in thermal compressible flows with the lattice Boltzmann method. *J. Fluid Mech.* **964**, A14.

LIU, L., HE, G., WU, M., LIU, G., ZHANG, H., CHEN, Y., SHEN, J. & LI, S. 2023 Climate change impacts on planned supply-demand match in global wind and solar energy systems. *Nat. Energy* **8**, 870–880.

MAC DOWELL, N., FENNELL, P.S., SHAH, N. & MAITLAND, G.C. 2017 The role of CO_2 capture and utilization in mitigating climate change. *Nat. Clim. Change* **7** (4), 243–249.

MAQSOOD, K., MULLICK, A., ALI, A., KARGUPTA, K. & GANGULY, S. 2014 Cryogenic carbon dioxide separation from natural gas: a review based on conventional and novel emerging technologies. *Rev. Chem. Engng* **30** (5), 453–477.

NAQUASH, A., QYYUM, M.A., HAIDER, J., BOKHARI, A., LIM, H. & LEE, M. 2022 State-of-the-art assessment of cryogenic technologies for biogas upgrading: energy, economic, and environmental perspectives. *Renew. Sustain. Energy Rev.* **154**, 111826.

NOCITO, F. & DIBENEDETTO, A. 2020 Atmospheric CO_2 mitigation technologies: carbon capture utilization and storage. *Curr. Opin. Green Sustain. Chem.* **21**, 34–43.

PAN, C.X., LUO, L.S. & MILLER, C.T. 2006 An evaluation of lattice Boltzmann schemes for porous medium flow simulation. *Comput. Fluids* **35** (8–9), 898–909.

PAN, X.Q., CLODIC, D. & TOUBASSY, J. 2013 CO_2 capture by antisublimation process and its technical economic analysis. *Greenh. Gases: Sci. Technol.* **3** (1), 8–20.

REN, J. & KLOKER, M. 2022 Instabilities in three-dimensional boundary-layer flows with a highly non-ideal fluid. *J. Fluid Mech.* **951**, A9.

SAWANT, N., DORSCHNER, B. & KARLIN, I.V. 2021 Consistent lattice Boltzmann model for multicomponent mixtures. *J. Fluid Mech.* **909**, A1.

SAWANT, N., DORSCHNER, B. & KARLIN, I.V. 2022 Consistent lattice Boltzmann model for reactive mixtures. *J. Fluid Mech.* **941**, A62.

SHI, B.C. & GUO, Z.L. 2009 Lattice Boltzmann model for nonlinear convection-diffusion equations. *Phys. Rev.* E **79** (1), 016701.

SHI, Y.Y., WU, L. & SHAN, X.W. 2021 Accuracy of high-order lattice Boltzmann method for non-equilibrium gas flow. *J. Fluid Mech.* **907**, A25.

SOLOMON, B.D 2023 Intergovernmental panel on climate change (IPCC). In *Dictionary of Ecological Economics* (ed. B.M. Haddad), p. 302. Edward Elgar Publishing.

SONG, C.F., KITAMURA, Y. & LI, S.H. 2012*a* Evaluation of stirling cooler system for cryogenic CO_2 capture. *Appl. Energy* **98**, 49–501.

SONG, C.F., KITAMURA, Y. & LI, S.H. 2014 Optimization of a novel cryogenic CO_2 capture process by response surface methodology (RSM). *J. Taiwan Inst. Chem. Engrs* **45** (4), 1666–1676.

SONG, C.F., KITAMURA, Y., LI, S.H. & JIANG, W.Z. 2013 Analysis of CO_2 frost formation properties in cryogenic capture process. *Intl J. Greenh. Gas Control* **13**, 26–33.

SONG, C.F., KITAMURA, Y., LI, S.H. & OGASAWARA, K. 2012*b* Design of a cryogenic CO_2 capture system based on stirling coolers. *Intl J. Greenh. Gas Control* **7**, 107–114.

SONG, C.F., LIU, Q.L., DENG, S., LI, H.L. & KITAMURA, Y. 2019 Cryogenic-based CO_2 capture technologies: state-of-the-art developments and current challenges. *Renew. Sustain. Energy Rev.* **101**, 265–278.

SONG, C.F., LIU, Q.L., JI, N., DENG, S., ZHAO, J. & KITAMURA, Y. 2017*a* Advanced cryogenic CO_2 capture process based on stirling coolers by heat integration. *Appl. Therm. Engng* **114**, 887–895.

SONG, C.F., LIU, Q.L., JI, N., DENG, S., ZHAO, J., LI, Y. & KITAMURA, Y. 2017*b* Reducing the energy consumption of membrane-cryogenic hybrid CO_2 capture by process optimization. *Energy* **124**, 29–39.

SUN, R., TIAN, H., SONG, C.F., DENG, S., SHI, L.F., KANG, K. & SHU, G.Q. 2021 Performance analysis and comparison of cryogenic CO_2 capture system. *Intl J. Green Energy* **18** (8), 822–833.

SUSSKIND, L., CHUN, J., GOLDBERG, S., GORDON, J.A, SMITH, G. & ZAERPOOR, Y. 2020 Breaking out of carbon lock-in: Malaysia's path to decarbonization. *Front. Built Environ.* **6**, 21.

TUINIER, M.J., HAMERS, H.P. & VAN SINT ANNALAND, M. 2011*a* Techno-economic evaluation of cryogenic CO_2 capture—a comparison with absorption and membrane technology. *Intl J. Greenh. Gas Control* **5** (6), 1559–1565.

TUINIER, M.J. & VAN SINT ANNALAND, M. 2012 Biogas purification using cryogenic packed-bed technology. *Ind. Engng Chem. Res.* **51** (15), 5552–5558.

TUINIER, M.J., VAN SINT ANNALAND, M., KRAMER, G.J. & KUIPERS, J.A.M. 2010 Cryogenic CO_2 capture using dynamically operated packed beds. *Chem. Engng Sci.* **65** (1), 114–119.

TUINIER, M.J., VAN SINT ANNALAND, M. & KUIPERS, J.A.M. 2011*b* A novel process for cryogenic CO_2 capture using dynamically operated packed beds-an experimental and numerical study. *Intl J. Greenh. Gas Control* **5** (4), 694–701.

WANG, Q.L., HAN, D.Y., WANG, Z.M., MA, Q.S. & WANG, D.Y. 2019 Lattice Boltzmann modeling for hydrate formation in brine. *Chem. Engng J.* **366**, 133–140.

WANG, Y.N., PFOTENHAUER, J.M., ZHI, X.Q., QIU, L.M. & LI, J.F. 2018*a* Transient model of carbon dioxide desublimation from nitrogen-carbon dioxide gas mixture. *Intl J. Heat Mass Transfer* **127**, 339–347.

WANG, Z., SUI, Y., SALSAC, A.-V., BARTHÈS-BIESEL, D. & WANG, W. 2018*b* Path selection of a spherical capsule in a microfluidic branched channel: towards the design of an enrichment device. *J. Fluid Mech.* **849**, 136–162.

WILLSON, P., LYCHNOS, G., CLEMENTS, A., MICHAILOS, S., FONT-PALMA, C., DIEGO, M.E., POURKASHANIAN, M. & HOWE, J. 2019 Evaluation of the performance and economic viability of a novel low temperature carbon capture process. *Intl J. Greenh. Gas Control* **86**, 1–9.

XU, Q., DAI, X., YANG, J., LIU, Z. & SHI, L. 2022 Image-based modelling of coke combustion in a multiscale porous medium using a micro-continuum framework. *J. Fluid Mech.* **932**, A51.

XU, Q.H., LONG, W., JIANG, H., MA, B., ZAN, C., MA, D.S. & SHI, L. 2018*a* Quantification of the microstructure, effective hydraulic radius and effective transport properties changed by the coke deposition during the crude oil in-situ combustion. *Chem. Engng J.* **331**, 856–869.

XU, Q.H., LONG, W., JIANG, H., ZAN, C., HUANG, J., CHEN, X. & SHI, L. 2018*b* Pore-scale modelling of the coupled thermal and reactive flow at the combustion front during crude oil in-situ combustion. *Chem. Engng J.* **350**, 776–790.

ZHANG, L.M., ZHANG, C.D., ZHANG, K., ZHANG, L., YAO, J., SUN, H. & YANG, Y.F. 2019 Pore-scale investigation of methane hydrate dissociation using the lattice Boltzmann method. *Water Resour. Res.* **55** (11), 8422–8444.

ZHANG, T., SHI, B.C., GUO, Z.L., CHAI, Z.H. & LU, J.H. 2012 General bounce-back scheme for concentration boundary condition in the lattice-Boltzmann method. *Phys. Rev.* E **85** (1), 016701.

ZHOU, J., JIN, Z.H. & LUO, K.H. 2020 The role of brine in gas adsorption and dissolution in kerogen nanopores for enhanced gas recovery and CO_2 sequestration. *Chem. Engng J.* **399**, 125704.